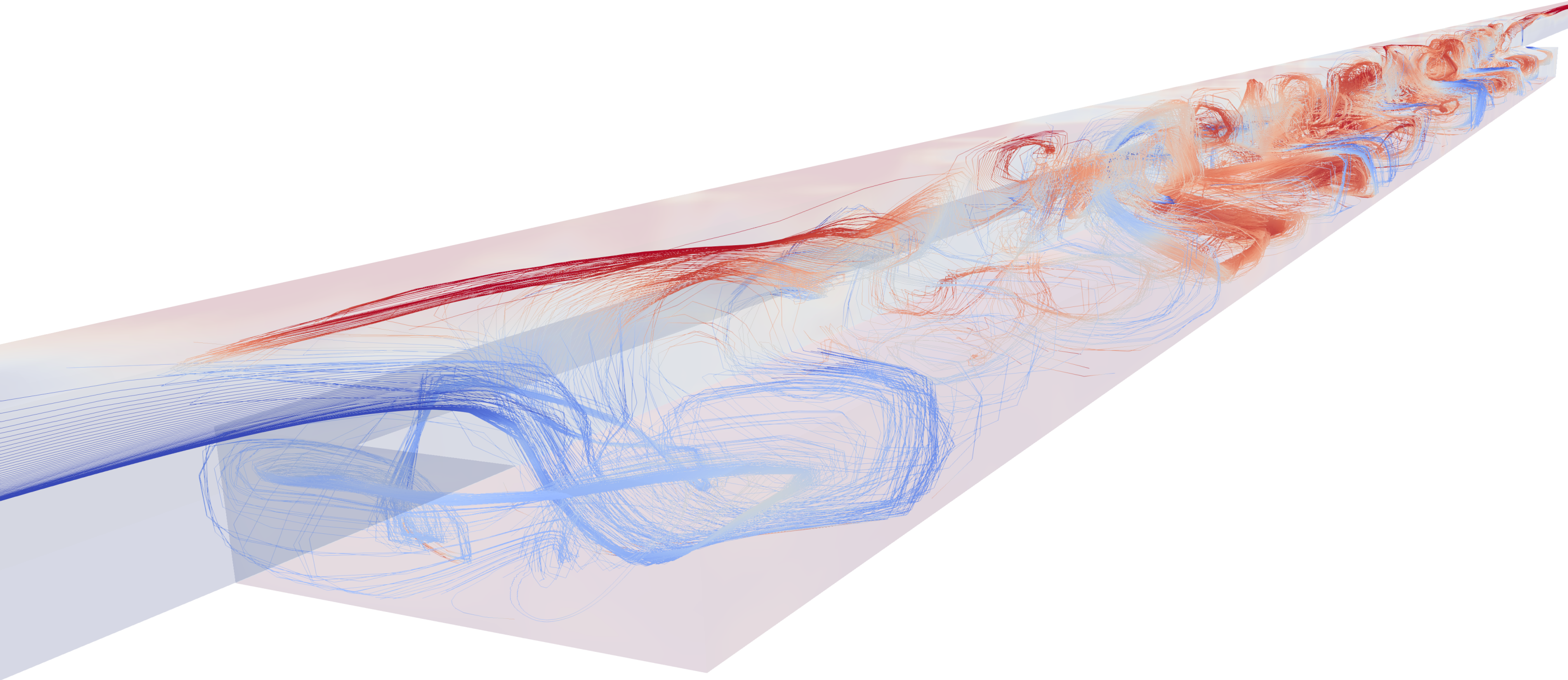

Proton Exchange Membrane Electrolyser Model in OpenFOAM

Rasmus D. Sørensen

AAU Energy, HYTEC-3 2023-12

STUDENT REPORT
AALBORG UNIVERSITY

List of software used in this project.

OpenFOAM® v2106:	For setting up and solving the computational fluid dynamics simulations.
ParaView 5.11.1:	For visualising the results.
MATLAB®:	For plotting and basic calculations.
LaTeX:	For typesetting the report, the official template of Aalborg University was used.
CoolProp	For determining thermophysical properties.

AALBORG UNIVERSITY
STUDENT REPORT

AAU Energy
Aalborg University
Pontoppidanstræde 111
http://www.aau.dk

Title:
Proton Exchange Membrane Electrolyser Model in OpenFOAM

Theme:
Master thesis

Project Period:
Spring Semester 2023

Project Group:
HYTEC4-1012

Participants:
Rasmus D. Sørensen

Supervisors:
Torsten Berning
Jakob Hærvig
Diogo Martinho

Page Numbers: 49

Date of Completion:
June 1, 2023

Abstract:

Hydrogen production is transitioning from fossil-based sources to electrolysis. Three major electrolysis technologies exist today, alkaline, proton exchange membrane (PEM) and solid oxide. In the period 2020-2030, PEM systems are expected to be the preferred technology.
Most of the CFD studies regarding PEM electrolysers are done using commercial software. Today there is a lack of suitable solvers in open-source code, such as OpenFOAM.
A two-phase, Euler-Euler model, solving the continuity equation and momentum equations for each phase, is expanded to include the generalised Darcy law and capillary pressure. The capillary pressure is modelled using the van Genuchten model. The interfacial forces include drag, turbulent dispersion and virtual mass.
The effects of the porous layer are investigated by varying the permeability, where it is concluded that the porous layer resulted in the phases becoming more mixed. The model is tested in different flow regimes. The stratified flow regime can be identified on inspection, but a VOF model is needed to clearly distinguish the other regimes. The inclusion of the lift force and heat transfer is also investigated, and it is concluded that neither has a significant effect on the fluid behaviour. Phase change is evaluated analytically, where it is concluded that up to 38.5 % of the total volume flow could consist of vapour and the cooling from evaporation corresponded to up to 20 % of the heat released due to the overpotential.

Summary

Hydrogen production is transitioning from fossil-based sources to electrolysis. Three major electrolysis technologies exist today, alkaline, proton exchange membrane (PEM) and solid oxide. In the period 2020-2030, PEM systems are expected to be the preferred technology, as they offer superior intermittent behaviour. Future challenges include improved gas, liquid and thermal management, which can be studied using CFD. Most of the CFD studies regarding PEM electrolysers are done using commercial software. Today there is a lack of suitable solvers in open-source code, such as OpenFOAM.

In this project, a two-phase, Euler-Euler model, solving the continuity equation and momentum equations for each phase, in OpenFOAM is expanded to include the generalised Darcy law and capillary pressure. The capillary pressure is modelled using the van Genuchten model. The interfacial forces include drag, turbulent dispersion and virtual mass. The developed model is then used to investigate the following:

- What effect does the porous layer have on the flow?
- Can the model identify different flow regimes?
- What effect does the lift force have on the flow?
- How does heat transfer affect the flow?

The effects of the porous layer are investigated by varying the permeability, where it is concluded porous layer results in the phases becoming more mixed.
The model is tested in different flow regimes. The stratified flow regime can be identified on inspection, but a VOF model is needed to clearly distinguish the other regimes.
The inclusion of the lift force and heat transfer is also investigated, and it is concluded that neither has a significant effect on the fluid behaviour. The change in

temperature was $\Delta T = 3.8$, and was well aligned with the analytically evaluated temperature change. In addition, an energy equation was solved for each phase, but the temperature difference between each phase was neglectable, meaning it could be considered to simplify the model by using a shared temperature field.
Phase change is not included, but is evaluated analytically, where it is concluded that up to 38.5 % of the total volume flow could consist of vapour and the cooling from evaporation corresponded to up to 20 % of the heat released due to the overpotential.

In future work, the model should be expanded to include phase change, as water vapour can be a significant part of the total volume flow. Other model developments can be the inclusion of an electrochemical model, in order to determine the current density distribution and the performance of the electrolyser.

Preface

This masters thesis project is written in the period of 1st February to 3rd of June 2023 at the Department of Energy Technology at Aalborg University.

Throughout the project, references are made using the Harvard method (Author, year). A list of all references can be found at the end of the report in the bibliography. Figures, tables and equations are numbered in order of their appearance and the chapter in which they appear (chapter number, no. equation of the chapter).

The developed models, the simulated cases and all the calculations done in the report can be found in the attachments or on GitHub.

I would like to thank my supervisors, Torsten Berning, Jakob Hærvig and Diogo Martinho for their helpful discussions and for always being available.

Aalborg University, June 1, 2023

Rasmus D. Sørensen
<rdsa18@student.aau.dk>

Nomenclature

Roman symbols	**Description**	**Unit**
A	Area	[m^2]
ASR	Area Specific Resistance	[Ω/m^2]
c	Constant	[-]
c	Specific heat capacity	[J/(kgK)]
C	Concentration	[mol/m^3]
Ca	Capillary Number	[-]
Co	Courant number	[-]
D	Diameter	[m]
D	Diffusion Coefficient	[m^2/s]
d	Diameter	[m]
e	Internal energy	[J/kg]
E	Reversible Cell Voltage	[V]
F	Faradays Constant	[C/mol]
Fr	Froude Number	[-]
$\boldsymbol{F}$	Force	[Pa/m]
$\boldsymbol{g}$	Gravitational acceleration vector	[m/s^2]
G	Mass flux	[kg/(m^{2}s)]
h	Enthalpy	[J/kg]
H	Enthalpy of Formation	[J/mol]
i	Current Density	[A/cm^2]
k	Thermal Conductivity	[W/(mK)]
K	Permeability	[m^2]
K	Taitel and Dukler Flow map parameter	[-]
k_{rel}	Relative permeability	[-]
m	Mass	[kg]
m	Van Genuchten fitting parameter	[-]
m	Taitel and Dukler flow map parameter	[-]
M	Molar mass	[kg/mol]
M	Momentum Source Term	[Pa/m]
M	Viscosity Ratio	[-]

n	integer	[-]
n	Moles	[mol]
n	Van Genuchten fitting parameter	[-]
n	Taitel and Dukler flow map parameter	[-]
$\boldsymbol{n}$	Normal vector	[-]
Nu	Nusselt Number	[-]
Pe_f	Flow Peclet number	[-]
p	Pressure	[Pa]
q	Heat Flux	[W/m^2]
r	Radius	[m]
$\boldsymbol{r}$	Position vector	[m]
R	Universal Gas Constant	[J/(molK)]
Re	Reynolds number	[-]
Re_p	Particle Reynolds number	[-]
Re_G	Shear Reynolds number	[-]
RH	Relative Humidity	[-]
s	Saturation	[-]
Sc	Schmidt number	[-]
Sh	Sherwood number	[-]
St	Stokes number	[-]
t	Time	[s]
T	Temperature	[K]
T	Taitel and Dukler Flow map parameter	[-]
$\boldsymbol{u}$	Velocity vector	[m/s]
u	Velocity	[m/s]
V	Voltage	[V]
V	Volume	[m^3]
V	Superficial velocity	[m/s]
X	Martinelli parameter	[-]
Y	Mass fraction	[-]
(x, y, z)	Cartesian coordinates	[m]

Greek symbols	**Description**	**Unit**
α	Volume phase fraction	[-]
α	Charge transfer coefficient	[-]
Γ	Volume-specific mass flow rate	[kg/(m^{3}s)]
ϵ	Dimensionless particle size	[-]
ε	Volume Porosity	[-]
η	Cell Voltage Losses	[V]

λ	Stoichometric Flow Ratio	[-]
λ	Baker Flow Map Parameter	[-]
μ	Dynamic viscosity	$[\mathrm{kg}/(\mathrm{m}\cdot\mathrm{s})]$
ν	Kinematic viscosity	$[\mathrm{m}^2/\mathrm{s}]$
ρ	Density	$[\mathrm{kg}/\mathrm{m}^3]$
σ	Prandtl number	[-]
σ	Surface tension	[N/m]
τ	Stress tensor	$\mathrm{kg}/(\mathrm{s}^2\mathrm{m})$
ϕ	Variable	[-]
ψ	Baker Flow Map Parameter	[-]

Subscripts	**Description**
act	Activation
an	Anode
avg	Average
b	Brownian
c	Continuous
c	Capillary
c	Center
cat	Cathode
cb	Break-through capillary pressure
d	Dispersed
dm	Maximum packing
D	Drag
e	Effective
evap	Evaporation
g	Gas
h	History
ht	Heat transfer
hyd	Hydraulic
i	Species
i	Phase
in	Inlet
l	Liquid
l	Lift
max	Maximum
MEA	Membrane Electrode Assembly
mem	Membrane
mix	Mixture

out	Outlet
p	Particle
rel	Relative
rev	Reversible
rgh	Density, gravity, height
sat	Saturation
t	Turbulent
tD	Turbulent dispersion
tot	Total
trans	Mass transfer
v	Vapour
V	Virtual mass
irr	Irreducible
0	Reference value

Superscripts	**Description**
$+$	Dimensionless
$'$	Fluctuating Component
$\cdot$	Flow
$\circ$	Standard conditions
eff	Effective

Operator	**Description**
-	Spatial mean operator
$\langle\rangle$	Temporal mean operator

Acronyms	**Description**
AEC	Alkaline Electrolysis Cell
BC	Boundary Conditions
CapEx	Capital Expenditures
CFD	Computational Fluid Dynamics
CL	Catalyst Layer
GDL	Gas Diffusion Layer
IC	Initial Conditions
MPL	Micro Porous Layer
LHV	Lower Heating Value
OpEx	Operating Expenditures
PEMEC	Proton Exchange Membrane Electrolysis Cell
PIMPLE	Merged acronym of PISO and SIMPLE

PISO	Pressure Implicit with Splitting of Operators
PTL	Porous Transport Layer
PtX	Power-to-X
RANS	Reynolds Averaged Navier Stokes
SIMPLE	Semi-Implicit Method for Pressure Linked Equations
SOEC	Solide Oxide Electrolysis Cell
SOFC	Solide Oxide Fuel Cell
STP	Standard Temperature Pressure
VOF	Volume of Fluid

Contents

Chapter 1

Introduction

In 2016, the Paris Agreement came into effect as an international legally binding treaty focused on climate change. The primary objective of this agreement is to limit the increase in global average temperature to below 2°C compared to pre-industrial levels (1850-1900) (UNFCCC, 2015). Concurrently, the European Union aims to reduce CO2 emissions by 40 % relative to 1990 levels by 2030 and ultimately achieve climate neutrality by 2050 (EU, 2021).

To reach the goals of UNFCCC (2015) and EU (2021), a transition from fossil-based energy sources to renewable sources is needed. This involves energy sources such as wind and solar to produce electricity. However, wind and solar are fluctuating and weather-dependent, requiring energy storage solutions. Excess electricity can be used for power-to-X (PtX) processes, which involve the electrolysis of water for hydrogen production. Hydrogen can then be used either directly as a fuel or refined into other hydrogen-based products (Araya et al., 2020). According to a study by A.P. Moller - Maersk and Lloyds Register (2019), the three main fuels in the future are alcohol, biomethane, and ammonia, where alcohol and ammonia are hydrogen-based products. Figure 1.1 illustrates the hydrogen demand from 1975 to 2018, and the hydrogen production by method in 2018 (IEA, 2019).

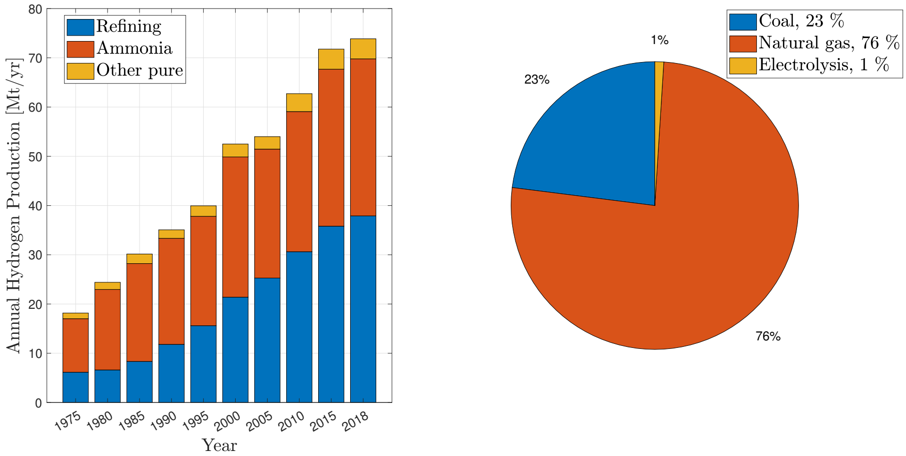

Figure 1.1: Left figure is the annual demand for hydrogen since 1975, right figure is the hydrogen production by method in 2018 IEA (2019).

Nearly all of the hydrogen is based on fossil fuels, resulting in the production being responsible for 830 $MtCO_2/yr$. To produce green hydrogen, it must be produced by electrolysis using electricity from renewable energy sources (IEA, 2019). If all the hydrogen produced in 2018 were to be produced by electrolysis, this would increase the annual electricity demand by 3600 TWh and water demand by 617 mio. m^3, which is more than the annual electricity production of the EU and twice the water consumption for hydrogen production from natural gas (IEA, 2019).

There are three major types of electrolyser technologies, alkaline electrolysis (AEC), proton exchange membrane electrolysis cell (PEMEC), and solid oxide electrolysis cell (SOEC). An overview of the technologies is given in table 1.1 (Grigoriev et al., 2020).

Electrolysis Technology	Alkaline	Proton Exchange Membrane	Solide Oxide
Operating Pressure	1-30 bar	30-80 bar*	1 bar
Operating Temperature	60-80 °C	50-80 °C	650-1000 °C
Operating hours	60-90,000	30-90,000	10-30,000
Electrical efficiency (LHV)	0.63-0.70	0.56-0.60	0.74-81
CapEx	1400 USD/kW_e	1800 USD/kW_e	5600 USD/kW_e

Table 1.1: Overview of the most common electrolysis technologies and key attributes today (2020). The table is based on Grigoriev et al. (2020). *Commercial PEMEC at operating pressures up to 700 bar already exists (HONDA, 2019).

The most common and mature technology is alkaline, which was commonly used until the production of hydrogen from steam reforming was developed, and the SOEC is the least mature technology. In the period 2020 to 2030 the preferred technology is expected to shift from AEC to PEMEC as costs are expected to be lowered with production scale-up and (IEA, 2019) (Schmidt et al., 2017). The PEMEC also has the advantage, compared to the other two technologies, of a higher load flexibility, which will be beneficial for balancing the electrical grid (Grigoriev et al., 2020) (Schmidt et al., 2017).

In Grigoriev et al. (2020), research trends and challenges in water electrolysis technologies are reviewed. The objectives are to increase current density, in order to decrease CapEx and increase efficiency to decrease OpEx. Future challenges include compactness, improved gas, liquid and thermal management, high load flexibility, durability and maintainability. The next section gives an overview of the research on the flow field in the PEMEC.

1.1 State of the Art

In Olesen et al. (2015) a numerical study is done on the flow and temperature maldistribution on the anode side. Two models are developed: a single-phase model for highlighting geometry effects on maldistribution and a two-phase model for understanding the effect of the gas-liquid flow interaction on maldistribution. The single-phase model solved steady-state volume-averaged equations of continuity, momentum and energy conservation. The momentum source term is equal to Darcy's law in the porous domain and zero elsewhere. Turbulence is modelled using the SST $k - \omega$ model. The Euler-Euler approach is used for the two-phase model, solving two sets of equations, one for the liquid phase and one for the gas phase. Interfacial transport terms are used for coupling between the phases, including the drag and turbulent dispersion force in the flow domain and Darcy's generalised law in the porous domain. The model assumes uniform current density and heat generation and neglects phase change and crossover of species. Key conclusions from the study included that a water stoichiometry of above 350 at a current density of 1 $\mathrm{A/cm^2}$ was required to avoid excessive heat spots and maldistribution could be reduced by approaching equal in-plane cross-sectional land area sizes. However, no experimental validations for the model had been done yet.

In Han et al. (2017) a steady-state, isothermal, two-phase model is developed for the porous domain in a PEMEC, taking electrochemical relations into account. The conservation of momentum for gas and liquid is modelled using Darcy's law and the Leverett function is used to model the capillary pressure. The model is used to investigate the two-phase flows effects on cell performance. Some of the conclusions from the study were that an increased contact angle in the GDL raises the voltage and decreases the efficiency, but an increased porosity will lower the voltage and increase efficiency.

In Lafmejani et al. (2017) a transient, multiphase CFD model is developed for studying the gas-liquid flow through an interdigitated anode flow field of PEMEC. The two-phase flow is modelled using the volume of fluid (VOF) method. The model is simplified by only considering the anode side flow channels and transport layers and neglecting electrochemistry. The model has several assumptions, e.g. uniform bubble generation, isothermal flow and dissolution of air in water is neglected. The governing equations solved are the conservation of momentum and continuity and volume fraction, with shared velocity and pressure for all phases. Turbulence is modelled using the SST $k - \omega$ model. Surface tension is modelled using the Continuum Surface Force model. The constructed model was validated by a qualitative comparison of pictures from an experimental setup. It was concluded that long Taylor bubbles, approaching annular flow, appeared to make the liquid flow more uniform. However, a more detailed CFD model is required to better capture the effects within the PEMEC.

The literature study in Olesen et al. (2019) concluded there was a lack of full-scale modelling, giving insight into how to achieve an even charge, mass and heat distribution. In Olesen et al. (2019), the model developed in Olesen et al. (2015) is improved upon, by including more physical phenomena. The developed model is stated to be the most comprehensive to date (2019). The model is solving the conservation of continuity, momentum, energy, species, electrons and ions. In addition, phase change, charge transport and reaction kinetics is included. A model is also applied to identify whether the flow is bubbly or slug. The computational domain is expanded to consist of the membrane, anode catalyst layer (CL), microporous layer (MPL), porous transport layer (PTL) and anode flow channel. Some of the main conclusions from the paper were, e.g., uniform, thin land width resulted in the most uniform temperature distribution and the locations with the highest current densities also had the highest temperatures and gas concentrations. However, further validation is required of the gas, temperature and current density fields.

In Wang et al. (2022) a new interdigitated-jet hole flow design is proposed to reduce temperature and reactant maldistribution. A three-dimensional, steady-state, non-isothermal and two-phase PEMEC model is developed, neglecting water evaporation, contact resistance between layers and crossover through the membrane. The Euler-Euler approach is used, and the continuity and momentum equations are solved in the anode and cathode flow fields, for the gas and liquid phase. The conservation equations for the current density are also solved to evaluate the polarisation curve. The main finding from the study is that the new design, on the anode side, would enhance mass and heat transfer and reduce maldistribution.

The presented studies have all used commercial software for the simulation of the PEMEC. Alternative open-source software does, however, exist. The next section will present the state of electrolyser and fuel cell studies using OpenFOAM.

1.2 Electrolysers and Fuel Cells using OpenFOAM

OpenFOAM is a open-source CFD software with various built-in solvers for different flow problems, such as two-phase and reacting flow. Most of the developed CFD models are developed using ANSYS, e.g. Olesen et al. (2015), Lafmejani et al. (2017) and Olesen et al. (2019). However, open-source code has the advantage, compared to commercial codes such as ANSYS, of being more flexible, as there is unlimited programmability and no license fees. In Beale et al. (2016), open-source code repositories for the modelling of Solide Oxide Fuel Cells (SOFC) were developed for OpenFOAM. The developed model calculated the local Nernst equation for open-circuit voltage, Kirchhoff-Ohm relationship for current distribution and considered local electro-chemistry fluid flow, multi-component species transport, and multi-region thermal analysis. However, the model does not consider two-phase flow, but this is built on in future publications (Beale and Lehnert, 2021).

Besides Beale et al. (2016), Beale and Lehnert (2021) describes the modelling procedures for electrochemical cells in OpenFOAM and builds on the existing structure of Beale et al. (2016). The book is mostly focused on the modelling of fuel cells (LT-PEMFC, HT-PEMFC, SOFC), but a simple 1D PEMEC model is also included. The PEMEC model is able to calculate the mass fraction of water and the current density across the length of the electrolyser as a function of the stoichiometric flow ratio (λ) and the reaction order (γ). For the more advanced fuel cell models, the two-phase Eulerian-Eulerian algorithm describes the flow. Like the SOFC model developed in Beale et al. (2016) the fuel cell is separated in different regions: two-phase flow channel, solid region, where only heat transfer is considered, electric region, where electric potential is calculated and finally the temperature is calculated globally for all regions. The setup for the advanced fuel cell models is, at the time of writing, not published yet. The presented results included e.g. current density distribution, polarisation curves, water saturation and oxygen distribution.

In the papers by Arbabi et al. (2016) and Rho et al. (2020) CFD models for PEMEC were developed in OpenFOAM.

In the paper by Arbabi et al. (2016), a transient two-phase CFD model is developed to predict oxygen bubble propagation in the PTL. The VOF method is used for multiphase modelling, solving the non-dimensionalised forms of the continuity and momentum equations. The model assumes incompressible fluids, isothermal behaviour and neglects gas density variation. Surface tension is modelled using the Continuum Surface Force model. A partial-slip boundary condition was used to simulate the hydrophilic titanium surface, with a slip velocity of 25% of the free-stream velocity. The results were validated using previous numerical results. The model can be used to design the PTL for oxygen gas removal. The solver used appears to be an unmodified solver of the OpenFOAM library.

In the paper by Rho et al. (2020), a transient CFD model was developed and validated using experimental data. This model aimed to address a limitation of previous models, which lacked a description of the interaction between the two-phase flow and the electrochemical reaction occurring in the membrane, referencing e.g. Olesen et al. (2015) and Olesen et al. (2019). The model was used to compare serpentine and parallel channels. At the anode, a two-phase model using the Euler-Euler approach is used, solving the continuity and momentum conservation equations, including the interfacial forces, drag, lift and turbulent dispersion, and at the cathode side, a single-phase model is used, where the Carman-Kozeny equation was used as a source term. To couple the model with an electrochemical model, a volume flux is specified as a function of the current density at the boundary between the anodes PTL and membrane. The main findings from the study included that the current density became more maldistributed at higher values and the serpentine channels had a slightly better performance than the parallel. Nothing in regards to fluid behaviour in the porous domain was however mentioned.

In the standard library of OpenFOAM, flow in a porous medium is modelled by adding a source term to the momentum equation, where different models can be chosen, among Darcy-Forchheimer. However, the model lacks elements such as phase saturation, relative permeability models, capillary models and specific boundary conditions Horgue et al. (2014). Code repositories for porous multiphase flow have been developed for OpenFOAM, namely *porousMultiphaseFoam* and *hybridPorousInterFoam*.

The toolbox *porousMultiphaseFoam* is described in the papers Horgue et al. (2014), Horgue et al. (2015) and Franc et al. (2016). The toolbox is developed for isothermal, incompressible two-phase flow with capillary effects, neglecting effects such as phase change and compressibility. The properties of each phase are considered homogenous inside each cell. The superficial velocity is determined for each phase using the generalised Darcy's model. The van Genuchten model and the Brooks and Corey model are available for the relative permeability. The same models are available for determining capillary effects as well as a linear model.

The toolbox *hybridPorousInterFoam* is described in the papers Carrillo and Bourg (2019), Carrillo et al. (2020) and Carrillo and Bourg (2021). The toolbox is developed for a single- and two-phase flow for a hybrid mesh consisting of a free and a porous domain. The multiphase in the free flow domain is modelled using the VoF method and in the porous domain, the generalised Darcy's law is solved.

From the literature study it is concluded that there is a lack of available PEMEC code in OpenFOAM, but previous work has already developed available code for fuel cells, which may also be useful for the PEMEC. This leads to the problem statement of this project.

From the literary study, it can be concluded that some CFD work regarding the flow in a PEMEC exists in OpenFOAM, but they all have drawbacks. In Arbabi et al. (2016) only the flow in the porous domain is described using the VOF method and in Rho et al. (2020) the model lacks a proper description of the flow in the porous domain. This leads to the problem statement.

1.3 Problem Statement

In the literature study, section 1.1 the approaches and main results of papers using CFD to investigate the flow in PEMECs are outlined. In section 1.2 OpenFOAM used in regards to electrolysers and fuel cells were reviewed. In Beale et al. (2016) and Beale and Lehnert (2021) comprehensive models were developed for fuel cells in OpenFOAM, but not yet for electrolysers.

In Arbabi et al. (2016) and Rho et al. (2020) electrolyser models were developed in OpenFOAM, but both had drawbacks. In Arbabi et al. (2016) a VOF model was developed focusing only on the porous layer and in Rho et al. (2020) a performance model was developed and two-phase flow was described using the Euler-Euler approach but lacked a description of the flow in porous domain.

Based on the literature study, PEMECs are almost purely simulated using commercial software and there is a lack of appropriate solvers in open-source CFD codes like OpenFOAM. The object of this project will therefore be to develop a two-phase model capable of including a porous layer in OpenFOAM, where the following questions are to be investigated:

- *What effect does the porosity have on the flow?*
- *How does the model behave in different flow regimes?*
- *How is the flow affected by the lift force?*
- *How does including heat transfer affect the flow?*

The considerations are restricted to the anode side in the PEMEC, where two-phase flow exists.

1.4 Structure of the Report

Figure 1.2 gives an overview of the arrangement of the report.

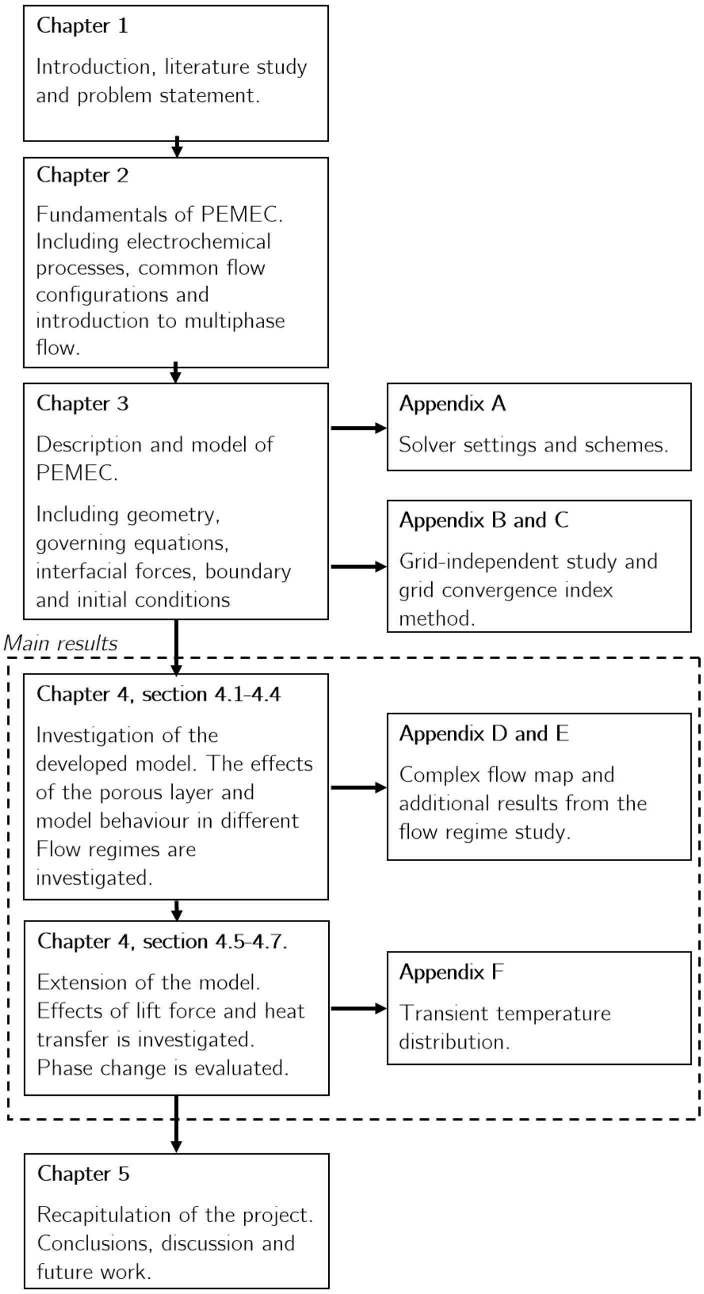

Figure 1.2: Overview of how the report is arranged.

Chapter 2

Proton Exchange Membrane Electrolyser Fundamentals

In this chapter, the general operation of a PEMEC is presented. This includes the electrochemical processes and flow patterns.

2.1 Electrochemical Process

A PEMEC is an electrochemical device producing hydrogen from the reaction described in equation (2.1) and (2.2) (Bessarabov et al., 2015).

$$H_2O \rightarrow \frac{1}{2}O_2 + 2H^+ + 2e^- \quad 2H^+ + 2e^- \rightarrow H_2 \tag{2.1}$$

$$H_2O \rightarrow \frac{1}{2}O_2 + H_2 \tag{2.2}$$

Where the left side of equation (2.1) is the anode half-reaction, the right side is the cathode half-reaction and equation (2.2) is the overall reaction. A cross-sectional view of a PEMEC is illustrated on figure 2.1.

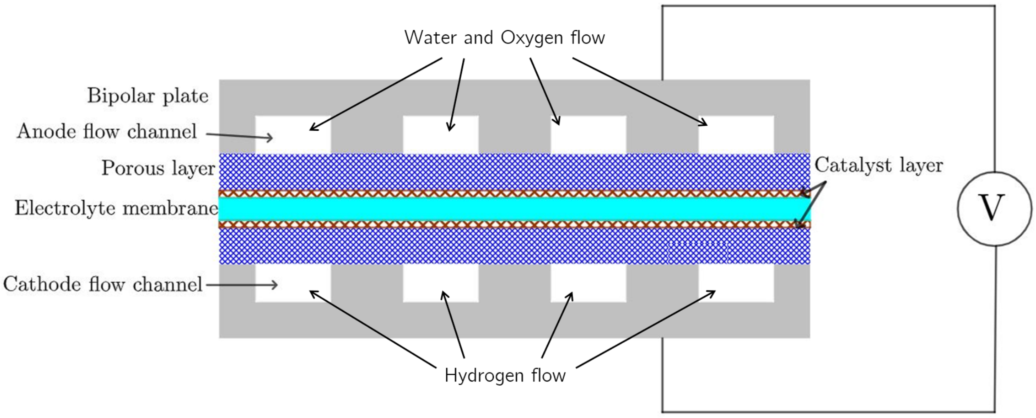

Figure 2.1: Cross-sectional view of a PEMEC. Inspired by Bang (2004).

The PEMEC consists of two electrodes, the anode and cathode, separated by the PEM. The electrodes and PEM are sandwiched by the bipolar plate. The porous layer can be split up into three layers, the PTL, the MPL and the CL (Olesen et al., 2019). The purpose of the porous layers is to improve the transport of reactants and products to and from the reaction sites and increase reaction surface area (O'Hayre et al., 2016). The catalyst layer is coated with a catalyst, where commonly used catalysts are platinum and iridium, and it is in this layer the reaction typically takes place (Shiva Kumar and Himabindu, 2019). Water flows on the anode side in the flow channels, which is split up into O_2, H^+ and $2e^-$, the membrane only allows for the protons to migrate, the oxygen molecules are mixed with the water flow and the electrons travel through the external electrical circuit. On the cathode side protons and electrons react, generating H_2. The membrane is typically made of Nafion®, as this is a material with a low gas permeability and high proton conductivity (Shiva Kumar and Himabindu, 2019).

In order for water to split up, a voltage higher than the cell voltage needs to be applied to the electrodes. This is commonly evaluated as equation (2.3) (Carmo et al., 2013).

$$V = E + \sum \eta_{\mathrm{i}} \tag{2.3}$$

Where V is the cell voltage, E is the reversible cell voltage and η_{i} is the different losses, including activation, mass transfer and ohmic. The thermodynamic reversible potential can be described by the Nernst equation (2.4) (Carmo et al., 2013).

$$E = E^0_{\mathrm{rev}} - \frac{RT}{2F} \ln \left(\frac{p_{\mathrm{H_2O}}/p}{(p_{\mathrm{H_2}}/p)(p_{\mathrm{O_2}}/p)^{1/2}} \right) \tag{2.4}$$

Where E_{rev}^{0} is the reversible potential at STP, R is the universal gas constant, F is Faradays constant, T is the temperature and p is the pressure. The activation losses can be described by the Butler-Volmer equation, given for the anode and cathode respectively in equation (2.5) (Carmo et al., 2013).

$$\eta_{\mathrm{act,an}} = \frac{RT_{\mathrm{an}}}{\alpha_{\mathrm{an}}F}\text{arc sin h}\left(\frac{i}{i_{0,\mathrm{an}}}\right) \quad \eta_{\mathrm{act,cat}} = \frac{RT_{\mathrm{cat}}}{\alpha_{\mathrm{cat}}F}\text{arc sin h}(\frac{i}{i_{0,\mathrm{cat}}}) \tag{2.5}$$

Where α is the charge transfer coefficient, i is the current density and i_0 is the exchange current density. The mass transfer losses are the losses due to an excessive amount of reaction products at the catalyst site, blocking the reactants. The relationship at the anode and cathode side respectively can be described with equation (2.6) (Carmo et al., 2013).

$$\eta_{\mathrm{trans,an}} = \frac{RT_{\mathrm{an}}}{nF}\ln\frac{C_{\mathrm{O_2,mem}}}{C_{\mathrm{O_2,mem,0}}} \quad \eta_{\mathrm{trans,cat}} = \frac{RT_{\mathrm{cat}}}{nF}\ln\frac{C_{\mathrm{H_2,mem}}}{C_{\mathrm{H_2mem,0}}} \tag{2.6}$$

Where $C_{\mathrm{i,mem}}$ is the concentration of species i at the membrane and $C_{\mathrm{i,mem,0}}$ is a reference concentration (Carmo et al., 2013). The ohmic losses are described by Ohm's law, given in equation (2.7) (Carmo et al., 2013).

$$\eta_{\mathrm{ohm}} = i \cdot ASR_{\mathrm{tot}} \tag{2.7}$$

Where ASR_{tot} is the total area-specific electrical resistance.

The polarisation curve for an arbitrary PEMEC is illustrated in figure 2.2, using reference values from Carmo et al. (2013).

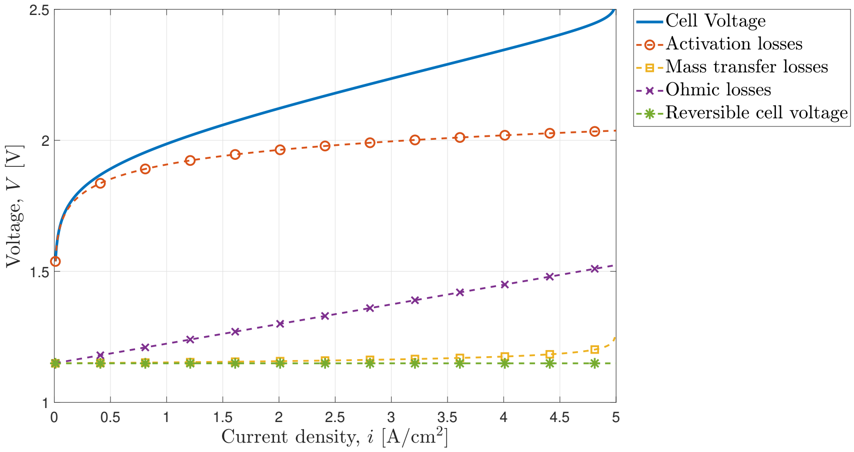

Figure 2.2: Polarisation curve for an arbitrary PEMEC.

2.2 Flow Configurations

In a PEMEC, several flow configurations can be used, the main three designs being parallel channels, interdigitated and serpetine (O'Hayre et al., 2016). Figure 2.3 illustrates these three flow configurations.

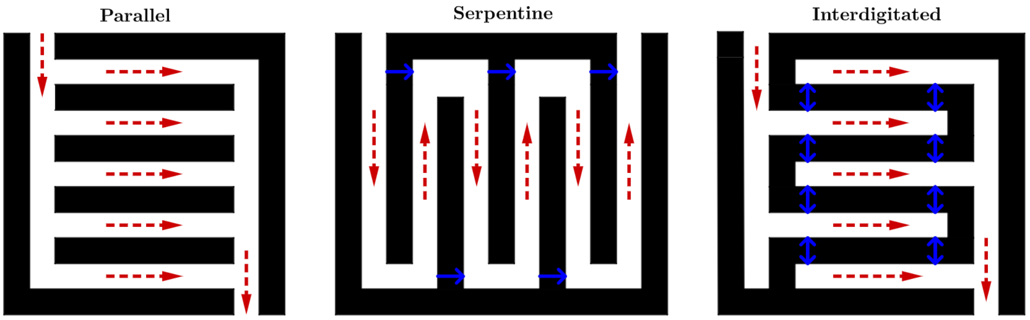

Figure 2.3: Common flow configurations encountered in PEMECs. Blue arrows denote cross-flow and red arrows bulk flow. Inspired by Bachman (2012).

The parallel design is the simplest design and has the lowest pressure drop. The disadvantage is however less uniform flow distribution. The serpentine design has improved water removal capability, but higher pressure drop. The interdigitated design forces cross-flow in the gas diffusion layer (GDL), promoting forced convection, but results in the highest pressure drop. In practice, combinations of each design are often used (O'Hayre et al., 2016).

2.3 Multiphase Flow

The flow on the anode side is a two-phase flow, consisting of mainly water and oxygen (Olesen et al., 2019). The cathode side is a single-phase flow, consisting of primarily hydrogen (Rho et al., 2020). As stated in the problem statement, section 1.3 on page 8, the purpose of this project is to develop a two-phase model with better porous treatment in OpenFOAM. This section presents flow patterns encountered in a horisontal pipe and the most common two-phase approaches and models.

In multiphase flow, several flow patterns are encountered. The different flow patterns for a horisontal pipe, which the PEMEC on the anode side can be simplified to, the flow patterns encountered are illustrated on figure 2.4 (Rasul et al., 2020).

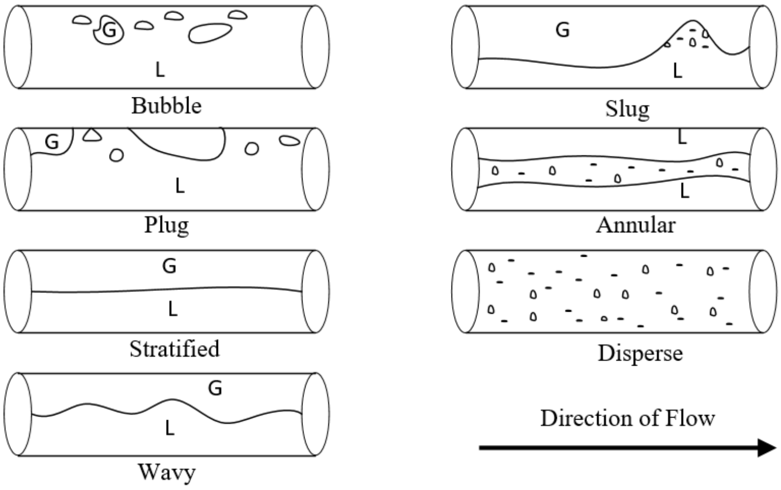

Figure 2.4: Flow patterns in a horisontal pipe (Rasul et al., 2020).

The flow patterns can be mapped using a flow pattern map. Figure 2.5 illustrates the original flow pattern map proposed by Baker (1954) for a horisontal pipe.

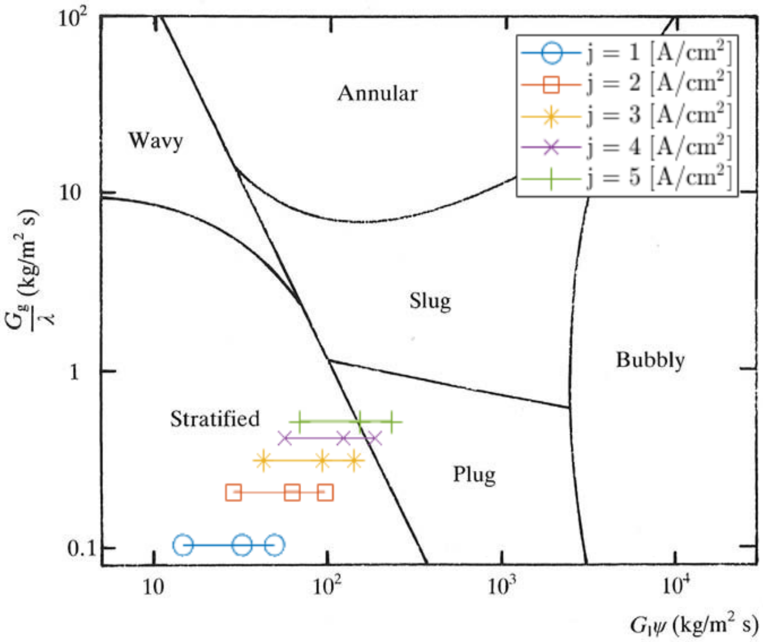

Figure 2.5: Flow pattern map for a horisontal pipe Baker (1954). G_i is the mass flux of phase i, λ and ψ are dimensionless parameters defined for the Baker map. The markers illustrate the expected flow regime for a current density of $1 < i < 5$ A/cm^2 and a stoichiometric flow ratio of $100 < \lambda < 350$.

Where the different markers illustrate the expected flow regime at the outlet given a stoichiometric flow ratio in the range of $100 < \lambda < 350$ and a current density of $1 < i < 5$ A/cm^2. The λ and ψ used in figure 2.5 are dimensionless parameters defined for the flow map, given as:

$$\lambda = \left(\frac{\rho_g}{\rho_g^\circ} \frac{\rho_l}{\rho_l^\circ} \right)^{1/2} \tag{2.8}$$

$$\psi = \frac{\sigma_l^\circ}{\sigma_l} \left(\frac{\mu_l}{\mu_l^\circ} \left[\frac{\rho_l^\circ}{\rho_l} \right]^2 \right)^{1/3} \tag{2.9}$$

Where σ is the surface tension and $^\circ$ refers to the value at standard conditions.

When modelling multiphase flows, two approaches can be used: Euler-Larange and Euler-Euler (Crowe, 2006). The Euler-Larange treats the fluid phase as a continuum and tracks a large number of particles, bubbles or droplets for the dispersed phase. The Euler-Euler approach introduces the phasic volume fraction and treats each phase of the flow as interpenetrating continua. A common model used for the Euler-Euler approach is the VOF, where the objective is to determine the position of the interface between the phases. The Euler-Euler approach is used in this project.

ANSYS, which is the most commonly used software for CFD modelling of PEMEC, has three different models available for the Euler-Euler approach: the VOF, mixture, and Eulerian (ANSYS, 2013). The VOF model is used for determining the position of the interface between immiscible fluids. A single set of momentum equations is solved and shared between the fluids. This is the model used by e.g. Lafmejani et al. (2017). The Mixture model solves a mixture momentum equation and prescribes relative velocities to describe the dispersed phases. The Eulerian model solves momentum and continuity equations for each phase. In Olesen et al. (2015) and Olesen et al. (2019) this model is used and coupling between the phases is achieved through interfacial transport terms. In OpenFOAM both VOF models, where a single set of momentum equations is solved and Eulerian models, where momentum and continuity equations are solved for each phase. An Eulerian model is used in this project.

In Guerrero et al. (2017), the Eulerian and VOF models are compared. The study's findings indicated that in order to achieve comparable error to the Eulerian model, the VOF model required ≈10 times more cells. This results in the VOF model having a higher computational demand. The VOF model is however better for predicting flow patterns.

Chapter 3

Numerical Methodology

In this chapter, the fundamental theory and considerations for the CFD model are presented. This includes presenting the geometry, relevant dimensionless numbers, the governing equations solved, interphase coupling and finally the applied boundary and initial conditions.

3.1 Geometry

Figure 3.1 illustrates the geometry and 3.2 is a sketch of the geometry in the z-plane.

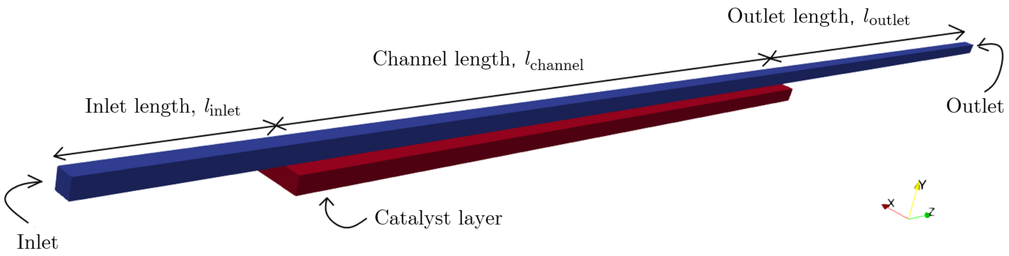

Figure 3.1: The computational domain, flow channel is marked as blue and the porous layer is marked as red.

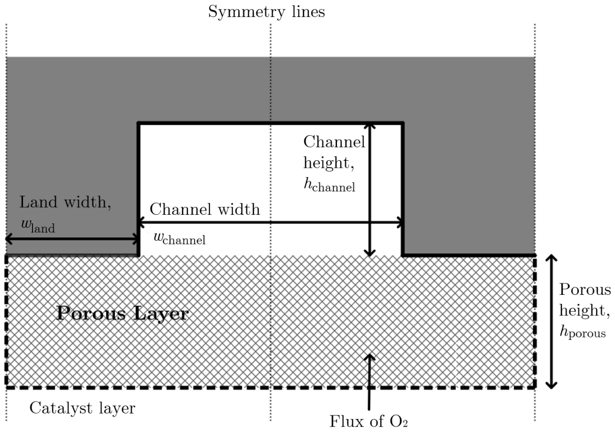

Figure 3.2: Sketch of a slice of computational demand, in the direction normal to z-plane.

The inlet and outlet, in figure 3.1, are extended. The inlet is extended to ensure the entering flow is fully developed. The outlet is extended to analyse the outlet flow patterns and to increase numerical stability. In order to differentiate between the porous and free flow domain, a switch is introduced, for activating and deactivating porous interactions. The value is 1 in the porous domain and 0 in the free-flow domain. The volume porosity $\varepsilon = 0.82$ in the porous domain and $\varepsilon = 1$ in the free-flow domain.

Table 3.1 gives an overview of the different geometrical inputs.

Parameter	Value	Parameter	Value
w_{land}	1 mm	w_{channel}	1 mm
h_{channel}	1 mm	h_{porous}	1 mm
l_{channel}	50 mm	l_{inlet}	10 mm
l_{outlet}	50 mm		

Table 3.1: Overview of geometrical inputs.

3.2 Dimensionless Numbers

This section presents and evaluates different relevant dimensionless numbers. This is done in order to decide which interphase forces to include and the flow regime in the porous domain. The dimensionless numbers are evaluated using the temporal averaged data from the grid-independent study, given in section 3.8.

3.2.1 Dimensionless Numbers for Interphase Forces

Several forces are neglected in this model, including forces such as lift and history. Table 3.2 gives an overview of the different forces, a description and their relative importance compared to the drag force, given in dimensionless parameters, based on the overview given in Hærvig (2017).

Force	Force description	Force ratio	Relative importance
Shear lift force	Lift induced by a velocity gradient	$F_\mathrm{l}/F_\mathrm{d}$	$\mathcal{O}(Re_\mathrm{G}^{1/2})$
Brownian force	Force due to the collision of small particles	$F_\mathrm{b}/F_\mathrm{d}$	$\mathcal{O}(1/(\epsilon St Pe_\mathrm{f})^{1/2})$
History force	Describes the force induced by a lagging boundary layer with a changing relative velocity	$F_\mathrm{h}/F_\mathrm{d}$	$\mathcal{O}(\epsilon Re St)^{1/2}$

Table 3.2: Description of different interphase forces and estimates of their relative importance (Hærvig, 2017).

Where Re_G is the shear Reynolds number, ϵ is the dimensionless particle size, St is the Stokes number and Pe_f is the flow Peclet number associated with Brownian motion (Hærvig, 2017). The dimensionless parameters are defined in the following equations:

$$Re = \frac{u D_\mathrm{hyd}}{\nu} \tag{3.1}$$

$$Re_\mathrm{G} = \frac{\rho_\mathrm{c} d_\mathrm{p}^2 \frac{du}{dy}}{\mu_\mathrm{c}} \tag{3.2}$$

$$\epsilon = d_\mathrm{p}/D_\mathrm{hyd} \tag{3.3}$$

$$St = \frac{\rho_\mathrm{p} d_\mathrm{p}^2 u}{18 \mu D_\mathrm{hyd}} \tag{3.4}$$

$$Pe_\mathrm{f} = \frac{u D_\mathrm{hyd}}{D_\mathrm{b}} \tag{3.5}$$

$$D_\mathrm{hyd} = \frac{4 A_\mathrm{c}}{p}$$

Where D_b is the Brownian diffusion coefficient, D_hyd is the hydraulic diameter, u is the velocity of the continuous phase, μ and ν is the dynamic and kinematic viscosity, d_p is the particle diameter, A_c is the cross-sectional area, p is the wetted perimeter and the subscripts c and d refers to the continuous and dispersed phase. Another dimensionless number often considered in multiphase flow is the particle Reynolds number Re_p, given as:

$$Re_\mathrm{p} = \frac{\rho_\mathrm{c}(|u_\mathrm{d} - u_\mathrm{c}|) d_\mathrm{p}}{\mu_\mathrm{c}} \tag{3.6}$$

Figure 3.3 illustrates Re_p and $Re_\mathrm{G}^{1/2}$ evaluated in the free flow domain.

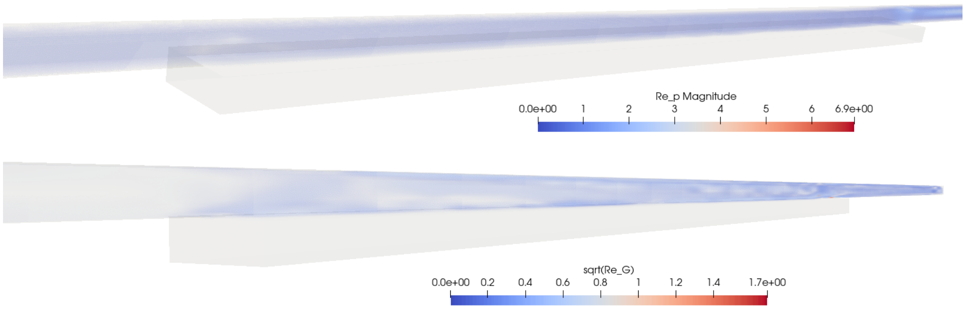

Figure 3.3: Top figure is Re_p and bottom is $Re_\mathrm{G}^{1/2}$ in the free flow domain.

The largest value of Re_p in the domain is $Re_{\mathrm{p,max}} = 6.9$, and in most of the domain the value is $Re_\mathrm{p} < 1$. According to Crowe (2006), the assumption that the bubble is spherical is acceptable until $Re_\mathrm{p} > 300$, meaning that for this case, the spherical assumption is acceptable. The mean value of $Re_\mathrm{G}^{1/2}$ is $(Re_\mathrm{G}^{1/2})_{\mathrm{avg}} = 0.09$ and the maximum value is $(Re_\mathrm{G}^{1/2})_{\mathrm{max}} = 1.7$ located near the walls. In section 4.5 on page 40 the lift forces are included to evaluate the effects on the flow.

Figure 3.4 illustrates the global values of ϵ, St, Pe_f and the relative importance of the Brownian and History force, as given in table 3.2.

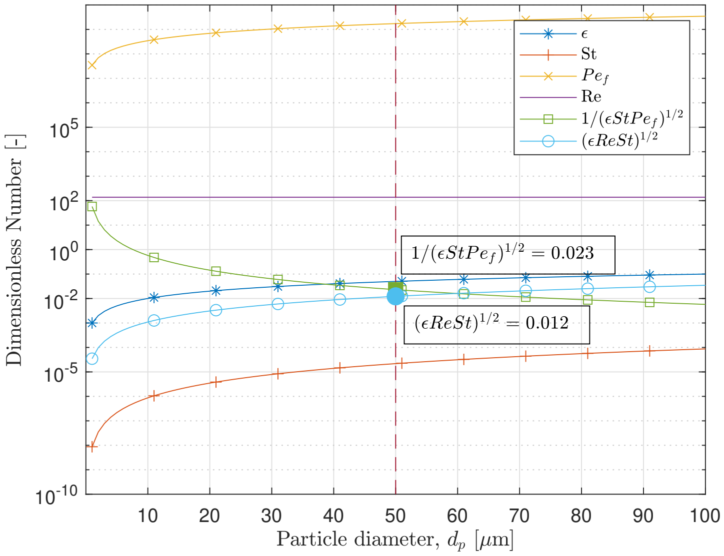

Figure 3.4: Global dimensionless numbers evaluated vs particle diameter, d_p.

At the selected value of $d_\mathrm{p} = 50 \cdot 10^{-6}$ m, the relative importance of both the History and Brownian force is in the order of $10-2$.

3.2.2 Dimensionless Numbers for the Porous Regime

When modelling the flow in a porous media, the capillary number ($Ca = u_\mathrm{g}\mu_\mathrm{g}/\sigma$) and viscosity ratio ($M = \mu_\mathrm{g}/\mu_\mathrm{l} = 0.07$) should be considered to identify the porous regime. In Lenormand (1990), three main regimes are identified. In short, the regimes are capillary fingering, the injection rate is low and viscous forces are negligible, viscous fingering, unstable displacement of viscous fluid by a less viscous fluid and stable displacement, viscous forces are high and capillary forces are negligible.

The capillary number is evaluated in the porous domain, to be in the range of $-6.9 < \log(Ca) < 0$, with a mean value of $\log(Ca)_\mathrm{avg} = -5$.

Figure 3.5 illustrates the phase diagram for the different regimes, based on Lenormand (1990) and Sinha and Wang (2007). The green dotted line presents the range calculated in the domain.

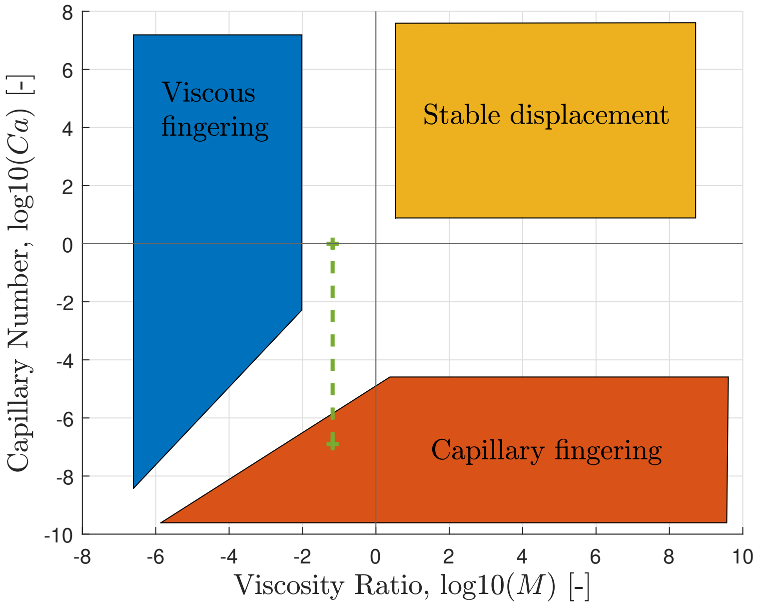

Figure 3.5: Phase diagram for flow in porous domain (Lenormand, 1990) (Sinha and Wang, 2007). The green dotted line represents the range calculated in the domain.

3.3 Governing Equations

The volume-averaged, macroscopic continuity and momentum conservation equations are solved for each phase, given in equation (3.7) and (3.8).

$$\frac{\partial}{\partial t}(\varepsilon\alpha_\text{i}\rho_i) + \nabla(\varepsilon\alpha_\text{i}\rho_\text{i}\boldsymbol{u}_\text{i}) = 0 \tag{3.7}$$

$$\frac{\partial}{\partial t}\varepsilon\alpha_\text{i}\rho_\text{i}\boldsymbol{u}_\text{i} + \nabla(\varepsilon\alpha_\text{i}\rho_\text{i}\boldsymbol{u}_\text{i}\boldsymbol{u}_\text{i}) = \varepsilon\alpha_\text{i}\rho_\text{i}\boldsymbol{g} - \varepsilon\alpha_\text{i}\nabla p - \varepsilon\alpha_\text{i}\nabla\tau_\text{i} + \varepsilon\alpha_\text{i}M_\text{i} \tag{3.8}$$

Where the subscript $i \in [l, g]$ denotes the phase, where l is the liquid phase and g is the gas phase, ε is the volume porosity, α is the phase volume fraction or total saturation in the porous medium, ρ is the density, $\boldsymbol{u}$ is the velocity vector, $\boldsymbol{g}$ is the gravitational acceleration vector, p is the shared pressure field, τ is the stress tensor and M is the momentum source terms. The governing equations have been modified from the original formulation in OpenFOAM (Busch, 2015) to match the governing equations described in Olesen et al. (2015), mainly by introducing ε.

The momentum source term is the momentum transfer between the phases. The momentum source term is given as stated in equation (3.9).

$$M_\text{i} = \begin{cases} \pm(\boldsymbol{F}_\text{Darcy} + \boldsymbol{F}_\text{D} + \boldsymbol{F}_\text{tD} + \boldsymbol{F}_\text{V}), & \text{Porous Layer} \\ \pm(\boldsymbol{F}_\text{D} + \boldsymbol{F}_\text{tD} + \boldsymbol{F}_\text{V}), & \text{Flow Channel} \end{cases} \tag{3.9}$$

Where $\boldsymbol{F}_\text{Darcy}$ is the generalised Darcy law, $\boldsymbol{F}_\text{D}$ is the interfacial drag force, $\boldsymbol{F}_\text{tD}$ is the turbulent dispersion force and $\boldsymbol{F}_\text{V}$ is the virtual mass force.

3.4 Porous Domain

The flow in the porous media is assumed to be in the viscous regime, and this is evaluated in 3.2. Based on this assumption, the porous forces are modelled as the generalised Darcy equation, given in equation (3.10).

$$F_\text{Darcy} = K^{-1}\frac{\mu_\text{i}\alpha_\text{i}\varepsilon}{k_\text{rel,i}}\boldsymbol{u}_\text{i} \tag{3.10}$$

Where K is the permeability, $k_{\text{rel},\alpha}$ is the relative permeability of phase i, μ is the dynamic viscosity. Physically, K is an area and is a measure of how connected the pores of a porous media are, where a high permeability means that the flow is less restricted compared to a low permeability (Lumen, 2023). The relative permeability, k_rel, is a variable introduced to account for multiphase flow in porous media and is the ratio of the effective permeability of phase i to the absolute permeability (Muskat et al., 1937). The parameter is a function of saturation and is modelled using the van Genuchten model, given in equation (3.11) and (3.12) (Gostick et al., 2006).

$$k_{\mathrm{rel,l}} = s_{\mathrm{e}}^{1/2}\left(1-(1-s_{\mathrm{e}}^{1/m})^{m}\right)^{1/2} \tag{3.11}$$

$$k_{\mathrm{rel,g}} = (1-s_{\mathrm{e}})^{1/3}(1-s_{\mathrm{e}}^{1/m})^{2m} \tag{3.12}$$

Where s_{e} is the effective saturation and m is a fitting parameter. The effective saturation is calculated using equation (3.13).

$$s_{\mathrm{e}} = \max\left(\frac{s-s_{\mathrm{irr}}}{1-s_{\mathrm{irr}}}, s_{\mathrm{irr}}\right) \tag{3.13}$$

Where $s = \alpha_{\mathrm{l}}$ is the liquid phase fraction corresponding to the total saturation (Nam and Kaviany, 2003) and s_{irr} is the irreducible saturation Olesen et al. (2022). A shared pressure field is used, which is acceptable in free flows, but in a porous layer capillary pressure needs to be accounted for (Olesen et al., 2015). The capillary pressure is defined as the pressure difference between the non-wetting phase and the wetting phase (Olesen et al., 2015). The van Genuchten model is used to model the capillary pressure, as in the papers Olesen et al. (2015) and Olesen et al. (2019), using the equation given in equation (3.14).

$$p_{\mathrm{c}} = p_{\mathrm{cb}}(s_{\mathrm{e}}^{-1/m}-1)^{1/n} \tag{3.14}$$

$$p_{\mathrm{g}} = p_{\mathrm{l}} + p_{\mathrm{c}} \tag{3.15}$$

Where p_{cb} and n are fitting parameters. Physically, p_{cb} corresponds to the breakthrough capillary pressure (Gostick et al., 2006). As in Olesen et al. (2015) it is assumed that the liquid phase pressure is solved for and the capillary pressure is added as a momentum source term for the gas phase, as stated in equation (3.16).

$$M_{\mathrm{g}} = -\nabla p_{\mathrm{c}} \tag{3.16}$$

The relative permeability of each phase and the capillary pressure as a function of the effective saturation is given in figure 3.6.

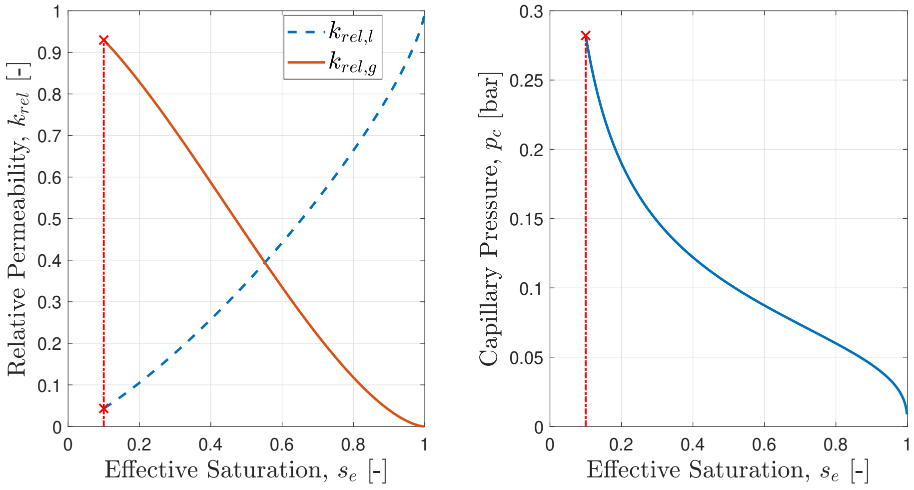

Figure 3.6: Left figure is the relative permeability of each phase, where the solid line is for the gas phase and the dashed line is for the liquid phase. The right figure is the capillary pressure. The red dash-dotted line marked with an x illustrates the point of irreducible saturation.

To avoid instability, an upper and lower limit is imposed on s_e, $-\nabla p_c$ and F_{Darcy}.

3.5 Interphase Coupling

In OpenFOAM, multiple models and constants must be specified for the interphase coupling. An overview of the selected interphase coupling is given.

3.5.1 Interphase Drag

The governing equations are solving for the velocity of two phases, the continuous liquid phase and the dispersed gas phase. This results in a drag force between the phases. The drag force can be modelled as stated in equation (3.17).

$$\boldsymbol{F}_D = \frac{1}{2} C_{\mathrm{D}} \rho_{\mathrm{c}} A |\boldsymbol{u}_{\mathrm{r}}| \boldsymbol{u}_{\mathrm{r}} \tag{3.17}$$

Where C_{D} is the drag coefficient, ρ_{c} is the density of the continuous phase, A is the projected area of the dispersed phase and $\boldsymbol{u}_{\mathrm{r}}$ is the relative velocity between the dispersed and the continuous phase, given as $\boldsymbol{u}_{\mathrm{r}} = \boldsymbol{u}_{\mathrm{d}} - \boldsymbol{u}_{\mathrm{c}}$. The area of the oxygen bubbles is based on the bubbles being spherical with a specified constant diameter.

The drag coefficient, C_{D} is modelled using the Ishii-Zuber model, a model developed for bubbly, droplet and particulate flows (Ishii and Zuber, 1979). The model for the drag coefficient in the stokes and viscous regime is given in (3.21) and (3.22) (Ishii and Zuber, 1979).

$$\mu_* = \frac{\mu_{\mathrm{d}} + 0.4\mu_{\mathrm{c}}}{\mu_{\mathrm{d}} + \mu_{\mathrm{c}}} \tag{3.18}$$

$$\frac{\mu_{\mathrm{mix}}}{\mu_{\mathrm{c}}} = \left(1 - \frac{\alpha_{\mathrm{d}}}{\alpha_{\mathrm{dm}}}\right)^{-2.5\alpha_{\mathrm{dm}}\mu_*} \tag{3.19}$$

$$Re_{\mathrm{p}} = \frac{d_{\mathrm{p}}\rho_{\mathrm{c}}|\boldsymbol{u}_{\mathrm{r}}|}{\mu_{\mathrm{mix}}} \tag{3.20}$$

$$\textit{Stokes regime:}\quad C_{\mathrm{D}} = \frac{24}{Re_{\mathrm{p}}} \tag{3.21}$$

$$\textit{Viscous regime:}\quad C_{\mathrm{D}} = \frac{24}{Re_{\mathrm{p}}}(1 + 0.1Re_{\mathrm{p}}^{0.75}) \tag{3.22}$$

Where α_{dm} is the maximum packing, which in the case of fluid-particle systems is set to α_{dm}=1, Re_{p} is the particle Reynolds number, d_{p} is the diameter of the dispersed particles and μ_{mix} is the mixture viscosity.

The particle diameter can be difficult to predict, but to simplify, the particle diameter is assumed to be constant at the same value of the characteristic pore diameter, as this is the limiting parameter inside the porous domain (Olesen et al., 2015).

3.5.2 Turbulent Dispersion

In multiphase flow, one of the phenomena that may occur is turbulent dispersion. The turbulence of one phase will affect the other phase, e.g., turbulence in the continuous phase results in regions of high concentration in the dispersed phase being transported to regions of low concentration (Burns et al., 2004).

In Olesen et al. (2015) a Favre averaged interphase drag model is used. In OpenFOAM, the Burns model is available, which is also a Favre averaged model. The Burns model, introduced in Burns et al. (2004), was first implemented in CFX-5 and validated for a variety of dispersed flows, including bubbly flows in vertical pipes. The implementation in OpenFOAM is discussed in Otromke (2013). The turbulent dispersion force is implemented in the following manner (Otromke, 2013).

$$\overline{M}_{\mathrm{td}} = -C_{\mathrm{td}}\frac{3}{4}\frac{\rho_{\mathrm{c}}\nu_{\mathrm{t}}}{d_p\sigma_{\mathrm{t}}}|\boldsymbol{u}_{\mathrm{r}}|\left(1 + \frac{\alpha_{\mathrm{d}}}{\alpha_{\mathrm{c}}}\right)\nabla\alpha_{\mathrm{d}} \tag{3.23}$$

Where C_{td} is a specified constant and σ_{t} is a specified turbulent Prandtl number (Otromke, 2013).

3.5.3 Virtual Mass

The virtual mass force is the force required to accelerate the fluid surrounding the particle. The force can be modelled as stated in equation (3.24) (ANSYS, 2013).

$$\boldsymbol{F}_{\mathrm{V}} = C_{\mathrm{V}} \frac{\rho_{\mathrm{c}}}{\rho_{\mathrm{d}}} \left(\boldsymbol{u}_{\mathrm{d}} \nabla \boldsymbol{u}_{\mathrm{c}} - \frac{\partial \boldsymbol{u}_{\mathrm{d}}}{\partial t} \right) \tag{3.24}$$

Where C_{V} is the virtual mass coefficient and is chosen to be $C_{\mathrm{V}} = 0.5$, as this is typically done (Norouzi, 2020), (ANSYS, 2013). The virtual mass force is only applied for water as the continuous phase and oxygen as the dispersed, as the virtual mass force is neglectable when $\rho_{\mathrm{c}}/\rho_{\mathrm{d}} << 1$.

3.5.4 Blending

In OpenFOAM it is necessary to specify how the solver should distinguish between the continuous and dispersed phases. A linear model is selected, where two constants, c_1 and c_2, are specified to define the boundaries of which phase is dispersed and continuous or whether a mixed solution is required. The principle is illustrated on figure 3.7.

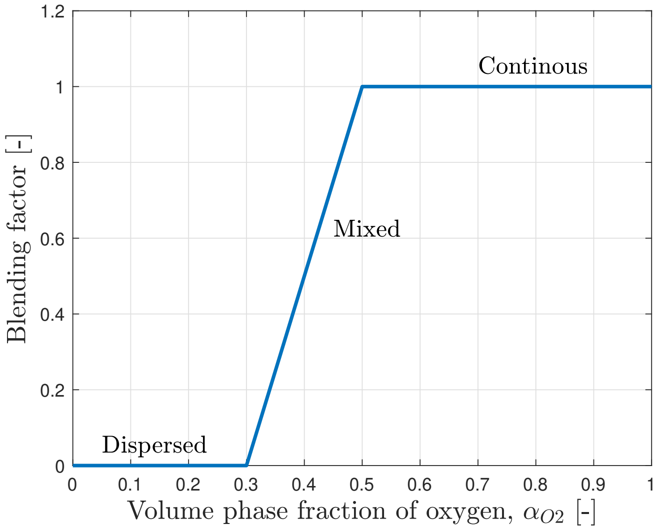

Figure 3.7: Blending factor, vs α_{O_2}. Inspired by Norouzi (2020).

This means if $\alpha_{\mathrm{g}} < c_1$ oxygen is considered as the dispersed phase, if $c_1 < \alpha_{\mathrm{g}} < c_2$ a mixed model is used and if $\alpha_{\mathrm{g}} > c_2$ water is considered as the dispersed phase.

In the case of a mixed state, a surface tension, σ, is specified.

3.6 Boundary and Initial Conditions

The applied boundary conditions (BC) and initial conditions (IC) are summarised in this section.

Table 3.3 gives an overview of the different BCs.

Parameter	Inlet	Outlet	Walls	Porous, sides	Porous, bottom	Front and Back
α_{O_2}	0	$\partial\phi/\partial\boldsymbol{n} = 0$	$\partial\phi/\partial\boldsymbol{n} = 0$	Symmetry	1	$\partial\phi/\partial\boldsymbol{n} = 0$
α_{H_2O}	1	$\partial\phi/\partial\boldsymbol{n} = 0$	$\partial\phi/\partial\boldsymbol{n} = 0$	Symmetry	0	$\partial\phi/\partial\boldsymbol{n} = 0$
p_{rgh}	$\partial\phi/\partial\boldsymbol{n} = 0$	1 bar	$\partial\phi/\partial\boldsymbol{n} = 0$	Symmetry	$\partial\phi/\partial\boldsymbol{n} = 0$	$\partial\phi/\partial\boldsymbol{n} = 0$
T_{O_2}	80 °C	$\partial\phi/\partial\boldsymbol{n} = 0$	$\partial\phi/\partial\boldsymbol{n} = 0$	Symmetry	$\partial\phi/\partial\boldsymbol{n} = 0$	$\partial\phi/\partial\boldsymbol{n} = 0$
T_{H_2O}	80 °C	$\partial\phi/\partial\boldsymbol{n} = 0$	$\partial\phi/\partial\boldsymbol{n} = 0$	Symmetry	$\partial\phi/\partial\boldsymbol{n} = 0$	$\partial\phi/\partial\boldsymbol{n} = 0$
u_{O_2}	$\partial\phi/\partial\boldsymbol{n} = 0$	$\partial\phi/\partial\boldsymbol{n} = 0$	0	Symmetry	Eq. (3.27)	0
u_{H_2O}	Eq. (3.26), parabolic profile	$\partial\phi/\partial\boldsymbol{n} = 0$	0	Symmetry	$\partial\phi/\partial\boldsymbol{n} = 0$	0

Table 3.3: Overview of key boundary conditions.

The assigned values are given in chapter 4 on page 31. The pressure field p is calculated at the boundaries based on p_{rgh}, which is a variable introduced to account for buoyancy. In OpenFOAM, the pressure gradient and gravity force terms are rearranged as stated in equation (3.25) (Greenshields, 2022).

$$-\nabla p + \rho \boldsymbol{g} = -\nabla p_{\text{rgh}} - (\boldsymbol{g} \cdot \boldsymbol{r}) \nabla \rho \tag{3.25}$$

Where $p_{\text{rgh}} = p - \rho \boldsymbol{g} \cdot \boldsymbol{r}$ and $\boldsymbol{r}$ is the position vector.

The velocity at the boundaries is calculated using equation (3.26) and (3.27), where equation (3.26) is at the inlet and equation (3.27) is at the bottom.

$$u_{\text{in,avg,H}_2\text{O}} = \frac{\dot{m}_{H_2O}}{A_{\text{inlet}} \rho} = \frac{M_{H_2O} \lambda i}{2 \rho_{H_2O} F} \tag{3.26}$$

$$u_{O_2} = \frac{\dot{m}_{O_2}}{A_{\text{MEA}} \rho_{O_2}} = \frac{M_{O_2} i}{4 \rho F} \tag{3.27}$$

Where λ is the stoichiometric flow ratio, A_{inlet} is the cross-sectional area of the inlet, A_{MEA} is the area of the membrane electrode assembly, M is the molar mass, j is the current density and F is Faraday's constant. At the inlet, a parabolic velocity profile is used to simulate a fully developed laminar flow. This is done using equation (3.28).

$$\begin{aligned} r_{\mathrm{x}} &= 1 - \left(\frac{x - x_{\mathrm{c}} + \Delta x_{\mathrm{displacement}}}{x_{\mathrm{c}}} \right)^4 \\ r_{\mathrm{y}} &= 1 - \left(\frac{y - y_{\mathrm{c}} + \Delta y_{\mathrm{displacement}}}{y_{\mathrm{c}}} \right)^4 \\ u_{\mathrm{in,z}}(x, y) &= 1.6 u_{\mathrm{in,avg,H_2O}} r_{\mathrm{x}} r_{\mathrm{y}} \end{aligned} \tag{3.28}$$

Where x and y are cartesian coordinates, x_{c} and y_{c} are the centre coordinate of the inlet, $\Delta x_{\mathrm{displacement}}$ and $y_{\mathrm{displacement}}$ are the inlet patch displacement from origo. Figure 3.8 illustrates the resulting velocity profile.

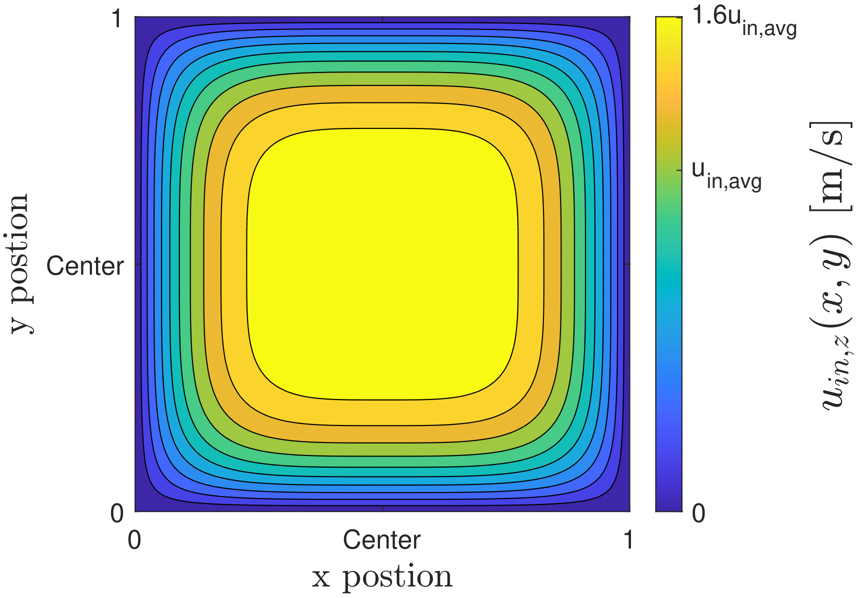

Figure 3.8: The velocity profile at the inlet.

The ICs are generated by solving for the flow field of the same geometry, but neglecting the porous zone. The base ICs for this case are given in table 3.4.

Parameter	Value
$\alpha_{\mathrm{O_2}}$	0
$\alpha_{\mathrm{H_2O}}$	1
p_{rgh}	1 bar
T_{i}	353 K
u_{i}	0 m/s

Table 3.4: Overview of base initial conditions.

3.7 Assumptions

The main assumptions of the model is listed below:

- Isothermal, a constant temperature of 80 °C is assumed.
- Uniform current density.
- Phase change of water is neglected.
- Cross-over of water, oxygen and hydrogen is neglected. All hydrogen is assumed to be on the cathode side, thus the gas-phase is currently assumed to be entirely oxygen.
- Water consumption is neglected.

3.8 Grid Independent Study

Three different grids are generated of 49, 110 and 208 thousand cells. The inputs used are given in table 4.1 on page 31 and the applied schemes and solver settings are given in appendix A on page 57. The parameters inspected for a grid-independent study are the phase volume fraction, velocity of each phase, and pressure distribution. To compare the difference in the results of the used grids, data is taken from a slice in the x-plane in the middle of the PEMEC, in the z-plane at the entrance to the outlet region and at the outlet of the domain. Based on the study, a grid of 208,000 cells is selected, details on the grid-independent study can be found in appendix B on page 59.

Chapter 4

Simulation Results and Discussion

This chapter presents the simulation results and assesses some of the model assumptions. This includes an introduction to the inputs used for the model, an inspection of the transient simulations to identify steady state, a study of the porous layer and different flow regimes, as well as the effects of lift and heat transfer on the flow and finally phase change is discussed.

4.1 Inputs

Table 4.1 gives an overview of the standard values used for different variables in the model.

Parameter	Value	Parameter	Value
i	$1\ \mathrm{A/cm^2}$	C_{td}	1
λ	350	σ_{t}	0.7
ε	0.82	c_1	0.3
K^{-1}	$2.25 \cdot 10^5\ \mathrm{m^{-2}}$	c_2	0.5
$s_{\mathrm{w,irr}}$	0.1	d_{bubbles}	$50\ \mu\mathrm{m}$
max s_{e}	0.999	d_{droplets}	$50\ \mu\mathrm{m}$
min/max ∇p_{c}	$\pm$ 10000 Pa/m	σ	0.0627 N/m
min/max $\mathbf{F}_{\mathrm{Darcy}}$	$\pm$ 10000 Pa/m		

Table 4.1: Overview of standard values for different variables used by the model.

Unless stated otherwise, these are the used values. In section 4.3 the effects of the porous layer are studied, using three different simulations where the following inputs are used:

Parameter	Simulation #1*	Simulation #2	Simulation #3
K^{-1}	-	$2.25 \cdot 10^5$ m^{-2}	$1 \cdot 10^{11}$ m^{-2}
ε	-	0.82	0.82

Table 4.2: Variations for the porous study in section 4.3. *Simulation does not include a porous layer.

In section 4.4 different flow regimes are simulated, achieved by varying i and λ as stated in table 4.3.

Parameter	Stratified	Plug	Slug
i	1 A/cm^2	0.89 A/cm^2	44 A/cm^2
λ	350	4398	88

Table 4.3: Variations for the flow regime study in section 4.4. Note that the values of i and λ may not be realistic for real applications.

4.2 Steady State

Figure 4.1 illustrates the normalised area-averaged values of $u_{\mathrm{H_2O}}$, $u_{\mathrm{O_2}}$ and $\alpha_{\mathrm{O_2}}$ at the outlet of the domain. The parameters are normalised by dividing with the time-averaged value.

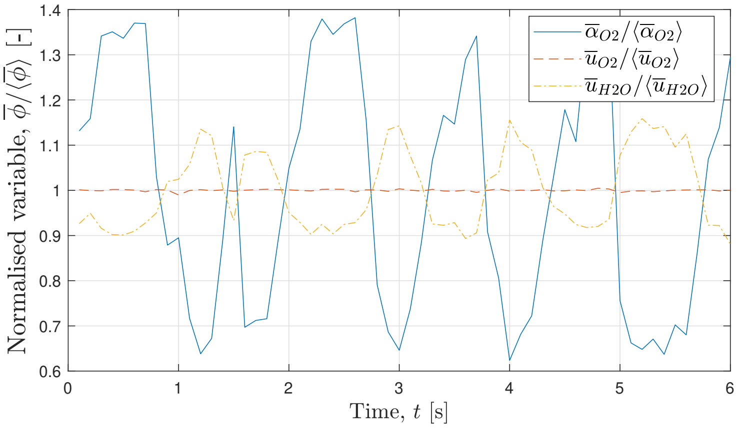

Figure 4.1: Normalised area averaged values of $u_{\mathrm{H_2O}}$, $u_{\mathrm{O_2}}$ and $\alpha_{\mathrm{O_2}}$ at the outlet of the domain.

From the figure, it can be concluded that no steady-state is achieved, but instead, a pseudo-steady-state, where the values fluctuate around a minimum and maximum value. This is common in multiphase flow, as a steady-state does not necessarily exist for the different flow regimes.

4.3 Effects of Porous Layer

In this section, the effects of the porous layer are evaluated by varying the permeability K. Three simulations are compared, a simulation with no porous layer, a simulation where $K = 2.25 \cdot 10^{-5}$ and a final simulation with $K = 1 \cdot 10^{-11}$.

Figure 4.2 illustrates the distribution of $\langle \alpha_{O_2} \rangle$ in the PEMEC, from a slice in the x-plane in the middle of the domain.

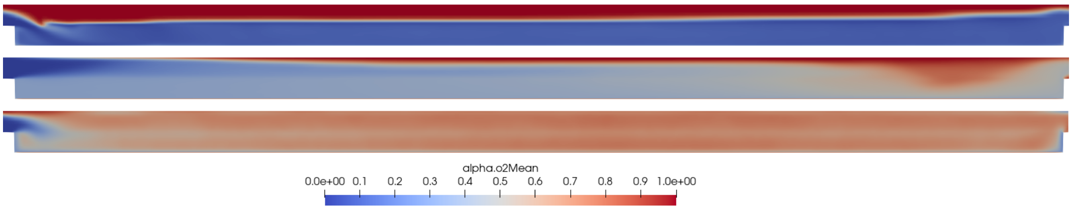

Figure 4.2: Time averaged volume phase fraction of oxygen. From top to bottom, no porous layer, $K = 2.25 \cdot 10^{-5}$ and $K = 1 \cdot 10^{-11}$.

The exclusion of the porous layer results in the flow becoming segregated in the PEMEC, whereas increasing the permeability results in the water and oxygen becoming more mixed.

Figure 4.3 illustrates the distribution of $\langle u_{O_2} \rangle$ in the PEMEC, from a slice in the x-plane in the middle of the domain.

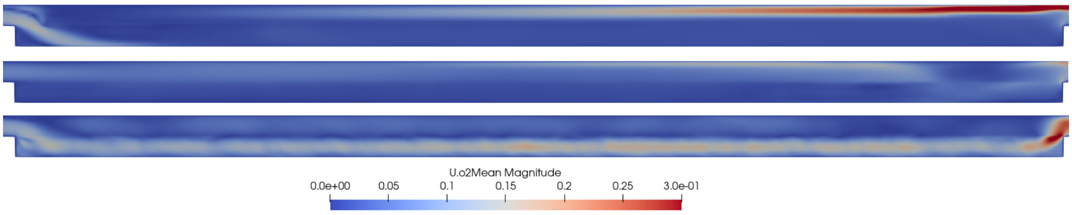

Figure 4.3: Time averaged gas velocity. From top to bottom, no porous layer, $K = 2.25 \cdot 10^{-5}$ and $K = 1 \cdot 10^{-11}$.

The most notable difference in the oxygen velocity distribution from figure 4.3 is a higher velocity at the top of the PEMEC when excluding the porous layer, a more even velocity distribution when $K = 2.25 \cdot 10^5$ and a higher velocity in the porous layer when $K = 2.25 \cdot 10^{11}$.

Figure 4.4 illustrates the distribution of $\langle u_{H_2O} \rangle$ in the PEMEC, from a slice in the x-plane in the middle of the domain.

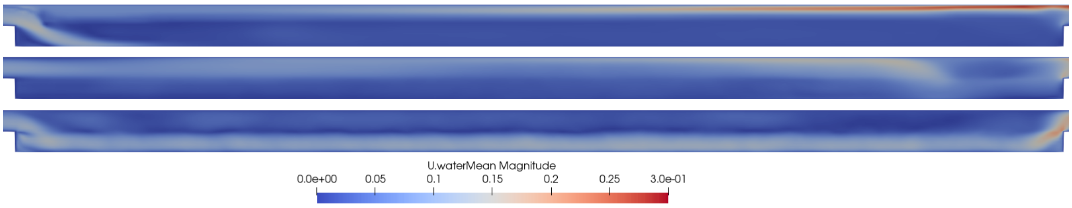

Figure 4.4: Time averaged liquid velocity. From top to bottom, no porous layer, $K = 2.25 \cdot 10^{-5}$ and $K = 1 \cdot 10^{-11}$.

Figure 4.4 illustrates the same effects on distribution of $\langle u_{H_2O} \rangle$ as figure 4.3 illustrated for $\langle u_{O_2} \rangle$. Excluding the porous domain results in a higher velocity at the top and increasing the permeability results in the distribution shifting towards the porous layer.

Figure 4.5 and figure 4.6 illustrate the distribution of $\langle p_g \rangle$ and $\langle p_l \rangle$ in the PEMEC, from a slice in the x-plane in the middle of the domain.

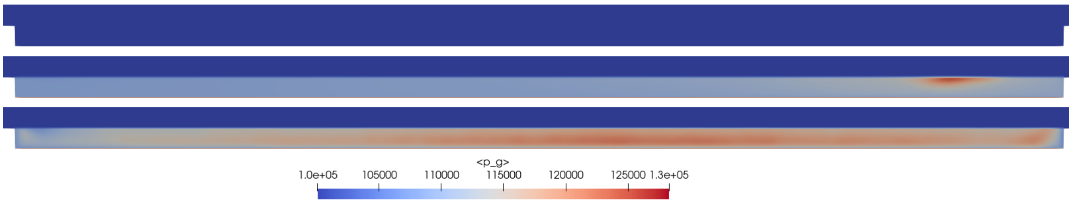

Figure 4.5: Time averaged pressure of the gas phase. From top to bottom, no porous layer, $K = 2.25 \cdot 10^{-5}$ and $K = 1 \cdot 10^{-11}$.

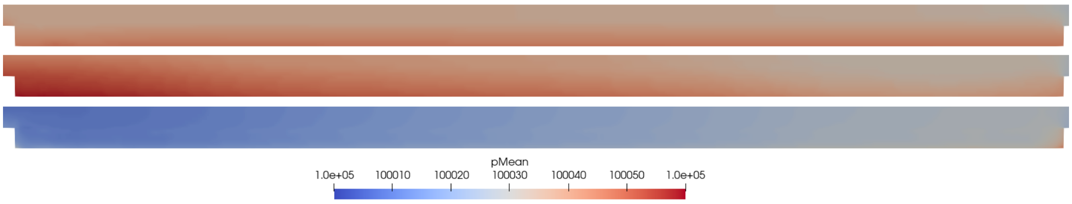

Figure 4.6: Time averaged pressure of liquid phase. From top to bottom, no porous layer, $K = 2.25 \cdot 10^{-5}$ and $K = 1 \cdot 10^{-11}$.

From figure 4.5, $\langle p_g \rangle$ increases in the porous layer as K increases. When excluding the porous layer capillary effects are not included and it is assumed $\langle p_g \rangle = \langle p_l \rangle$. The changes in the liquid pressure from each cash are very low, in the range of 10-20 Pa.

4.4 Flow Regime Study

To further test the limits of the developed model, the current density and stoichiometry are varied to evaluate the flow in different regimes. Figure 4.7 illustrates the different points evaluated.

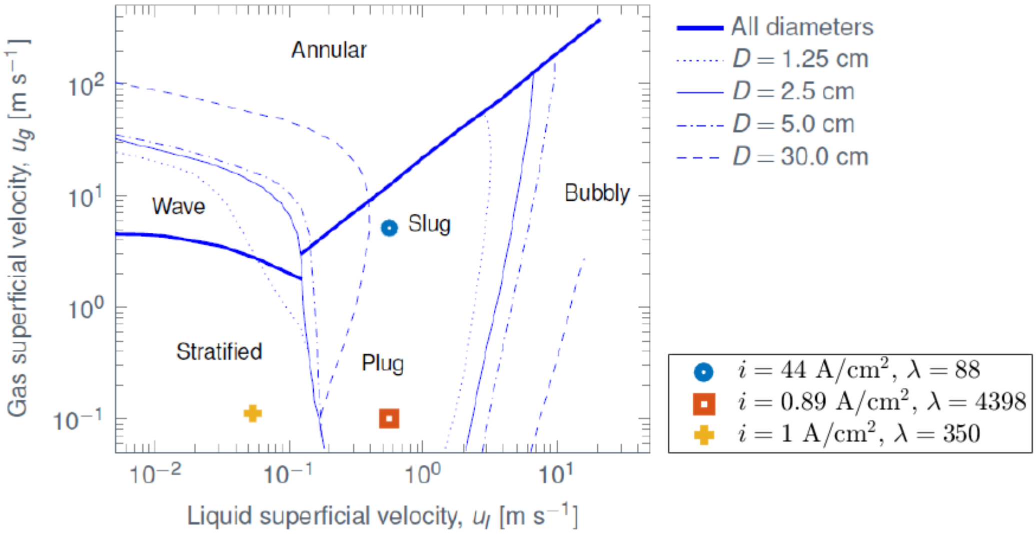

Figure 4.7: Flow pattern map for a horisontal pipe, from Olesen et al. (2019), originally propsed in Mandhane et al. (1974). Illustrating points tested by the model, and the corresponding value of i and λ to achieve that flow regime.

The values of i and λ may be unrealistic for real applications, but the purpose of these simulations is only to test the model behaviour. The flow patterns are also evaluated using the Taitel and Dukler map. The point determined to be in the slug and plug flow regime is determined to be in the annular and bubbly flow regime respectively when using the Taitel and Dukler flow map. The procedure and results are described in appendix D on page 65.

As multiphase flow, in most of these regimes, is inherently transient, the transient results are inspected. To identify patterns in the flow, the oxygen volume phase fraction is sampled along a line in the middle of the flow domain in the PEMEC for each simulation. Figure 4.8 illustrates the average, minimum, maximum and upper and lower quartile of α_{O_2} along the line for each simulation.

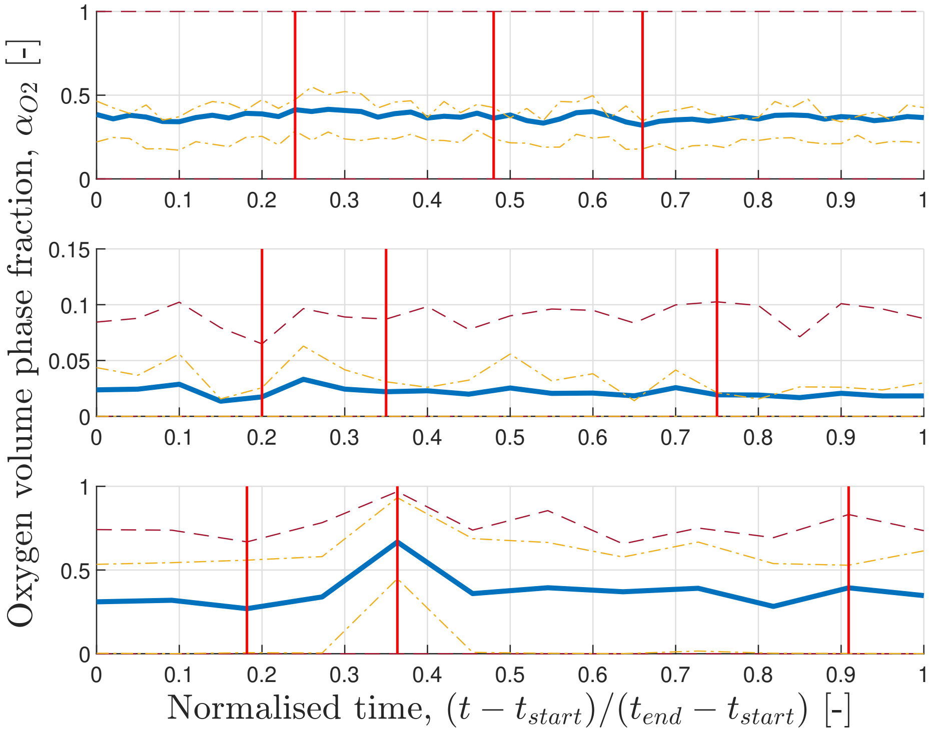

Figure 4.8: Volume phase fraction of oxygen in the middle of the PEMEC, from top to bottom: stratified, plug and slug. The solid lines are $\overline{\alpha}_{\mathrm{O}_2}$, the yellow dash-dotted lines are the lower and upper quartiles, and the red dashed lines are the minimum and maximum values. The vertical red lines represent the points that are to be inspected.

The points chosen for inspection are the points where α_{O_2} is high, low and a point in between the minimum and maximum. These points will be referred to as the minimum, mid and maximum point.

Figure 4.9, 4.10, 4.11 illustrates the phase volume fraction of α_{O_2} in the PEMEC, for the three simulated scenarios, stratified, plug and slug flow.

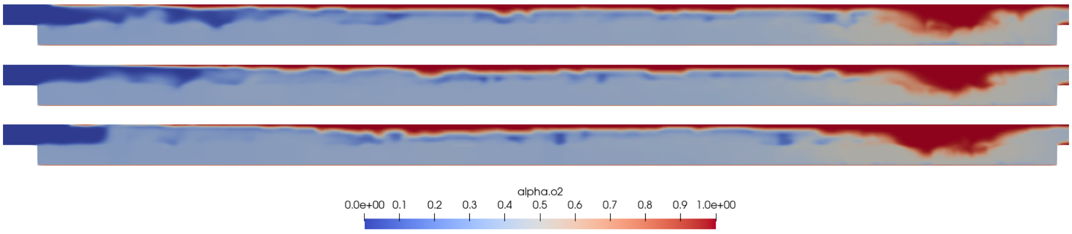

Figure 4.9: The transient flow inside the PEMEC, for the stratified flow. From top to bottom is the flow at the minimum, mid and maximum points. The parameter illustrated is α_{O_2}

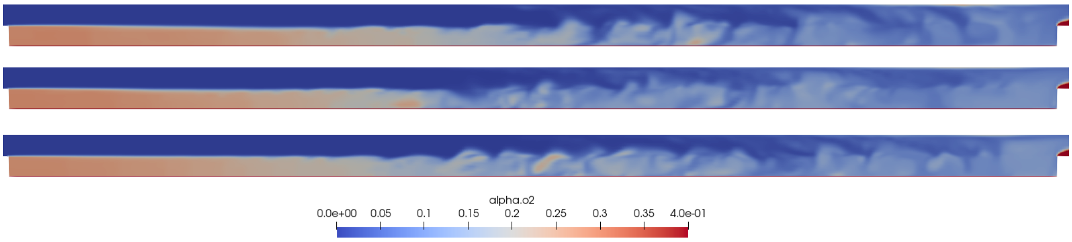

Figure 4.10: The transient flow inside the PEMEC, for the plug flow. From top to bottom is the flow at the minimum, mid and maximum point. The parameter illustrated is α_{O_2}.

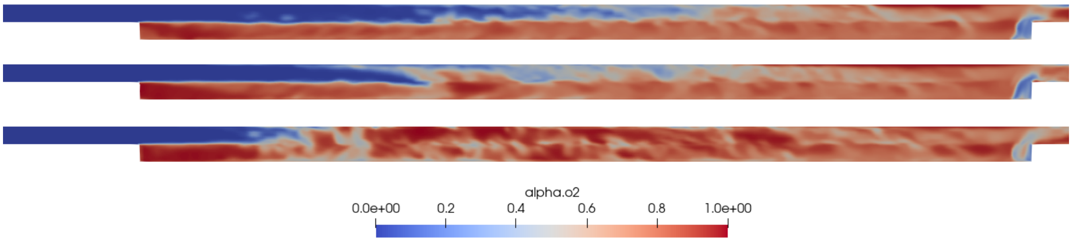

Figure 4.11: The transient flow inside the PEMEC, for the slug flow. From top to bottom is the flow at the minimum, mid and maximum point. The parameter illustrated is α_{O_2}.

In the stratified flow regime, a high concentration of oxygen occurs near the exit of the PEMEC region. The plug flow has the lowest oxygen concentration, which makes sense as the oxygen flow is unchanged from the stratified flow, but the liquid flow has increased by approximately a factor of 10. In the slug flow the distribution appears more well-mixed but with a generally higher concentration of oxygen than the other two.

Figure 4.12, 4.13, 4.14 illustrates the phase volume fraction of α_{O_2} in the outlet region of the computational domain, for the three simulated scenarios, stratified, plug and slug flow.

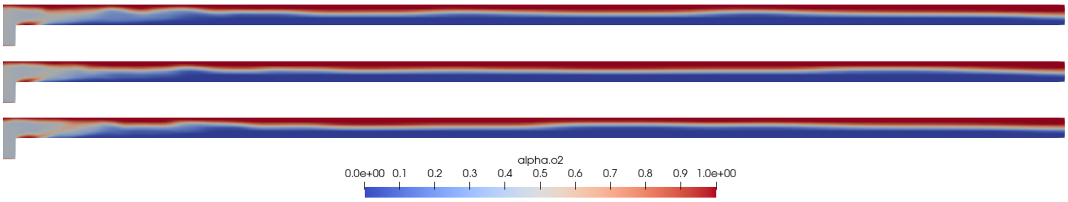

Figure 4.12: The transient flow at the outlet, for the stratified flow. From top to bottom is the flow at the minimum, mid and maximum point. The parameter illustrated is α_{O_2}.

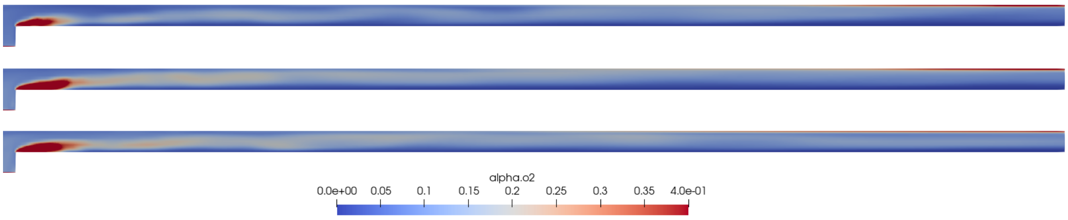

Figure 4.13: The transient flow at the outlet, for the plug flow. From top to bottom is the flow at the minimum, mid and maximum point. The parameter illustrated is α_{O_2}.

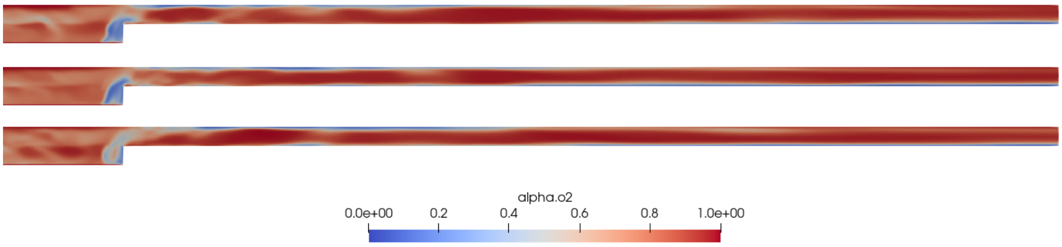

Figure 4.14: The transient flow at the outlet, for the slug flow. From top to bottom is the flow at the minimum, mid and maximum point. The parameter illustrated is α_{O_2}.

The stratified flow appears to have a clear transition between the gas and liquid phase. The interface between the phases appears wavy, but becomes more stable

as the outlet is reached.
The plug flow generally has a high concentration of water at the bottom and dispersed oxygen concentration in the middle and top. However, near the outlet high oxygen concentrations have assembled at the top of the pipe, characteristic of plug flow.
The slug flow, which was determined annular using the Taitel and Dukler flow map, the gas phase is dominating. As the outlet is reached, high oxygen concentrations are achieved at the top, and at the bottom, a small concentration of water is found. The characteristic of slug flow is a high wavy gas concentration at the top and middle and liquid at the bottom. In annular flow, the gas phase is in the middle, pushing the liquid phase to the sides. The flow regime can be hard to identify based on solely these results and to get a more clear distinction a VOF model can be used.

In appendix E on page 67 similar figures can be found for the velocity gas and liquid phase and the pressure field. The pressure drop for each case is given in table 4.4.

Flow regime	Stratified	Plug	Slug
Pressure drop	55 Pa	1965 Pa	5456 Pa

Table 4.4: Overview of pressure drop from inlet to outlet of each case.

The smallest and largest drop is in the stratified and slug flow regime, which is expected as this is the lowest and highest velocity respectively.

4.5 Effects of Lift Force

In section 3.2 the relative importance of the lift force was evaluated, to be in the order of $10^{-1} - 10^{0}$, compared to the drag force. A simulation is therefore carried out where the lift force is included, to see what effect this will have on the flow. The lift force is given as stated in equation (4.1)

$$\boldsymbol{F}_{\mathrm{l}} = C_{\mathrm{l}} \frac{\pi d_{\mathrm{p}}^{3}}{6} \rho_{\mathrm{c}} (\boldsymbol{u}_{\mathrm{r}} \nabla \boldsymbol{u}_{\mathrm{c}}) \tag{4.1}$$

Where C_{l} is the lift coefficient, which for simplicity is assumed to have a constant value of $C_{\mathrm{l}} = 0.25$. The lift model is only applied for water as the continuous phase and oxygen as the dispersed phase.

Figure 4.15 illustrates the distribution of $\langle \alpha_{O_2} \rangle$.

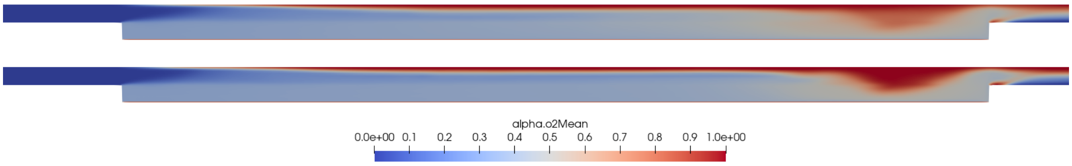

Figure 4.15: Time averaged oxygen volume phase fraction in the PEMEC. The bottom figure includes the lift force, and the top does not.

The distribution of $\langle \alpha_{O_2} \rangle$ is very similar in both scenarios, but with a slightly higher concentration of oxygen at the top when including the lift force. The velocity field and pressure field have also been inspected, but the inclusion of the lift force only resulted in minor differences.

4.6 Heat Transfer

The overall reaction in a PEMEC is endothermic, but when operating at a voltage higher than the equilibrium voltage, the reaction becomes exothermic. Following the thermodynamic analysis done in Olesen et al. (2015), the heat generated due to the overpotential can be evaluated as stated in equation (4.2).

$$q_{\text{reaction}} = (V_{\text{cell}} - \frac{\Delta H^{\circ}}{nF}) i_{\text{cell}} \tag{4.2}$$

Where q_{reaction} is heat flux and ΔH° is the standard enthalpy of formation.

Figure 4.16 illustrates the arbitrary polarisation curve from section 2.1 on page 11 using the left y-axis and the right y-axis is q_{reaction} vs the current density.

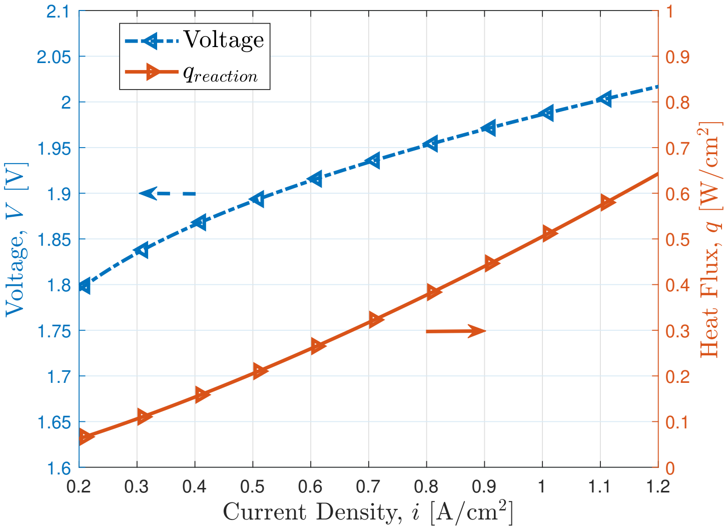

Figure 4.16: The left y-axis is the polarisation curve given in section 2.1 on page 11. The right y-axis is q_{reaction}. The figure is inspired by Olesen et al. (2015).

4.6.1 Implementation

The heat transfer associated with the electrochemical reaction is included by introducing a fixed temperature gradient boundary condition at the bottom of the porous domain. The gradient is specified normal to the boundary, as stated in equation (4.3).

$$\mathbf{q} = -k\nabla T \Rightarrow \frac{\partial T}{\partial \boldsymbol{n}} = \frac{q_{\text{reaction}}}{k} \tag{4.3}$$

Where k is the thermal conductivity at the boundary.

In OpenFOAM, the solver twoPhaseEulerFoam, which the solver used in this project is based on solves the total energy equation for each phase to describe the conservation of energy (Manni, 2014). The equation is modified to include ε and neglect mechanical work. The modified conservation of energy can be expressed as given in equation (4.4).

$$\frac{\partial}{\partial t}(\varepsilon\alpha_{\text{i}}\rho_{\text{i}}e_{\text{i}}) + \nabla(\varepsilon\alpha_{\text{i}}\rho_{\text{i}}\mathbf{u}_{\text{i}}e_{\text{i}}) = \nabla(\varepsilon\alpha_{\text{i}}\alpha_{\text{eff}}\nabla e_{\text{i}}) + K_{\text{ht}}\Delta T + S_{\text{i}} \tag{4.4}$$

Where e_{i} is the sensible enthalpy of phase i, α_{eff} is the effective thermal diffusivity, $K_{\text{ht}}\Delta T$ is the interphase heat transfer and S_{i} is the energy source term of phase i. In case of phase change being included, the energy source term could be the cooling done by the evaporation.

For the interphase coupling K_{ht} is determined using equation (4.5), using the Ranz-Marshall model.

$$K_{\mathrm{ht}} = 6\frac{k_{\mathrm{i}}\alpha_{\mathrm{i}}\alpha_{\mathrm{j}}Nu_{\mathrm{i}}}{d_{\mathrm{p}}^2} \qquad Nu_{\mathrm{i}} = 2 + 0.6Re_{\mathrm{p}}^{0.5}\sigma_{\mathrm{i}}^{0.33} \tag{4.5}$$

Where Nu is the Nusselt number and σ is the Prandtl number. The Ranz-Marshall model was developed for $Re_{\mathrm{p}} < 200$.

The thermophysical properties, e.g. μ, σ, c_{p} and c_{V}, are assumed constant, as only a small temperature range is expected.

4.6.2 Results

A simulation was done, with heat transfer implemented as discussed above. The initial and boundary conditions are updated to the following;

Parameter	Boundary Condition, Porous Layer	Initial Condition
T_{O_2}	$\partial T/\partial \boldsymbol{n} = 172 \cdot 10^3$ K/m	333 K
T_{H_2O}	$\partial T/\partial \boldsymbol{n} = 7682$ K/m	333 K

Table 4.5: Updated temperature boundary conditions for the simulation including heat transfer.

Where the previous boundary condition and initial condition were $\partial T/\partial \boldsymbol{n} = 0$ and $T = 353$ K respectively.

Figure 4.17 illustrates the distribution of $\langle \alpha_{O_2} \rangle$, where the top is when not including heat transfer, and the bottom does include heat transfer.

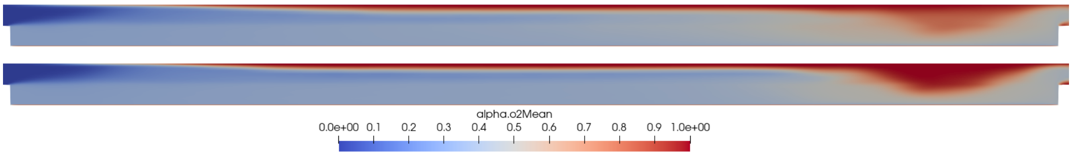

Figure 4.17: Distrubtion of $\langle \alpha_{O_2} \rangle$. The top figure does not include heat transfer, the bottom one does.

No major effects are found on the distribution of $\langle \alpha_{O_2} \rangle$, when including heat transfer. Figure 4.18 illustrates the temperature distribution in the computational domain for both oxygen and water.

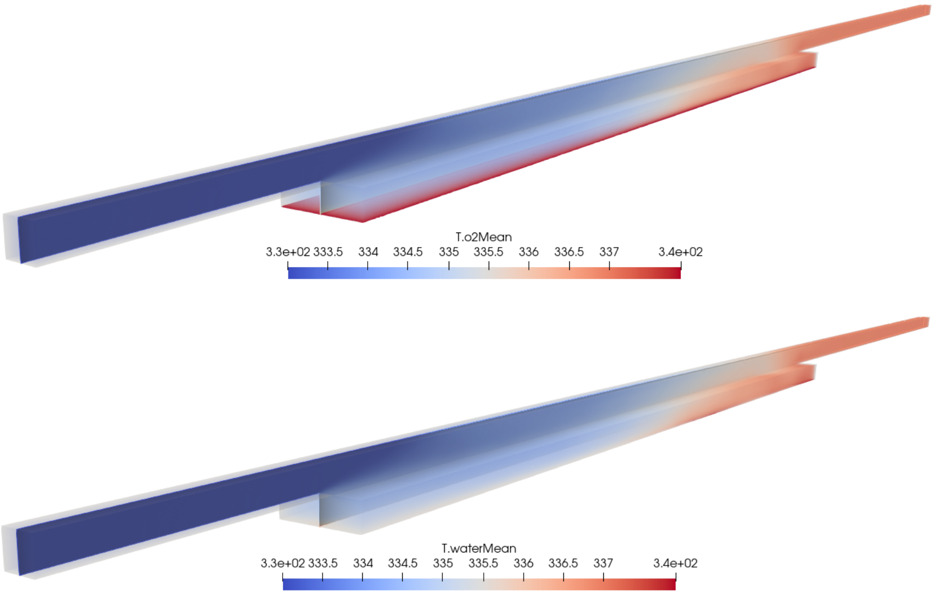

Figure 4.18: Temperature distribution in the computational domain. Top figure is T_{O_2}, bottom is T_{H_2O}.

The temperature distribution appears to be very similar for both oxygen and water. The main difference is a higher oxygen temperature at the porous layer. This makes sense, as this is where the heat flux is specified and there is also specified a boundary condition of $\alpha_{O_2} = 1$. Figure 4.19 illustrates the temperature distribution, in the porous region displayed in a histogram. The data has been interpolated to a uniformly distributed mesh.

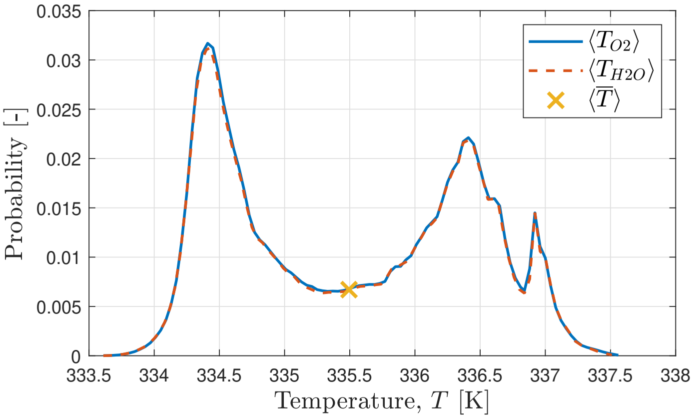

Figure 4.19: Histogram of temperature distribution for both oxygen and water, in the porous region. The marker 'x' marks the temporal and spatial average temperature in the porous region.

Based on these results, it could be considered to simplify the model and only use a single temperature field, as the temperature difference is low.

The fluids are heated from $T = 333$ K at the inlet to $T = 336.8$ K when entering the outlet domain, meaning a temperature change of $\Delta T = 3.8$ K. The temperature change is evaluated analytically in equation (4.6).

$$\Delta T = \frac{q_{\text{reaction}} A_{\text{MEA}}}{c_{\text{p,O}_2} \dot{m}_{\text{O}_2} + c_{\text{p,H}_2\text{O}} \dot{m}_{\text{H}_2\text{O}}} = 3.7 \text{ K} \tag{4.6}$$

Meaning the difference between the analytical and numerical is
$\Delta T_{\text{analytical,numerical}} = 0.1$ K.

In appendix F on page 73 the transient temperature distribution is inspected and compared to the time-averaged temperature distribution.

4.7 Phase Change

The current model neglects phase change. Using a similar procedure as described in Berning and Al Shakhshir (2016), the amount of water undergoing phase change can be estimated using equation (4.7).

$$RH_{\text{out}} = \frac{p_{\text{H}_2\text{O,out}}}{p_{\text{sat}}(T_{\text{out}})} = x_{\text{H}_2\text{O,out}} \frac{p_{\text{g,out}}}{p_{\text{sat}}(T_{\text{out}})} = \frac{\dot{n}_{\text{H}_2\text{O,out}}}{\dot{n}_{\text{H}_2\text{O,out}} + \dot{n}_{\text{O}_2\text{,out}}} \tag{4.7}$$

Where RH_{out} is the relative humidity at the outlet, p_{sat} is saturation pressure, $x_{\text{H}_2\text{O,out}}$ is the molar fraction of water vapour at the outlet and $\dot{n}_{\text{i}}$ is the molar flow. Assuming the oxygen is 100 % humidified, the maximum amount of water vapour can be estimated using equation (4.7). Besides the flow, heat transfer is also affected by phase change. The cooling effect from evaporation be evaluated using equation 4.8.

$$q_{\text{evap}} = \frac{\Delta h_{\text{evap,H}_2\text{O}} \dot{m}_{\text{vapour}}}{A_{\text{MEA}}} \tag{4.8}$$

Where q_{evap} is the cooling effect of the evaporation and $h_{\text{evap,H}_2\text{O}}$ is the enthalpy of evaporation of water.

On the left, figure 4.20 illustrates the ratio of the flow of oxygen, water vapour and liquid water, as well as the ratio of liquid water at the inlet and outlet as a function of λ. The right of figure 4.20 illustrates the ratio of $q_{\text{evap}}/q_{\text{reaction}}$ vs the current density.

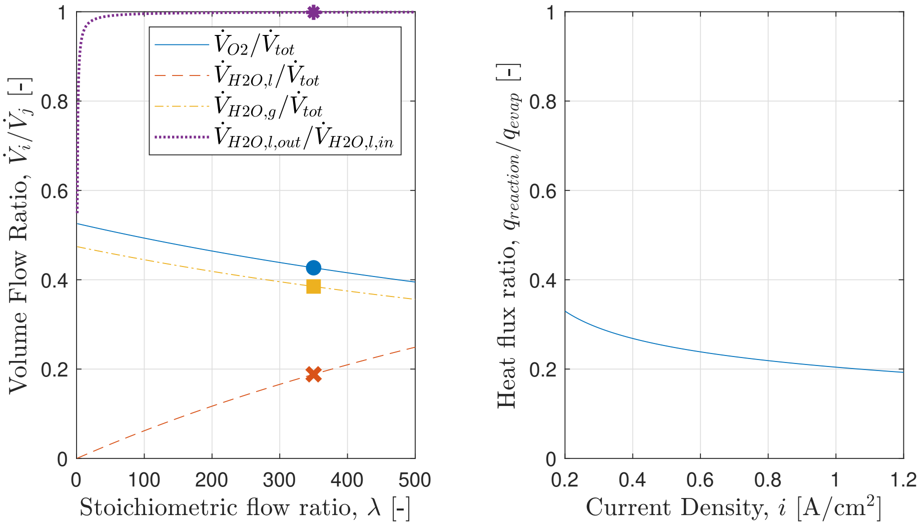

Figure 4.20: Left figure is the ratio of the volume flow of each gas and liquid to the total volume flow. The right figure is likewise, but with the mass flow instead. The points of $\lambda = 350$ are marked.

The phase change effect on the volume flow is quite significant, as up to 38.5 % of the total volume flow can consist of water vapour. The effect on the total flow of liquid water is low in almost any range (< 1 % when $\lambda > 45$)

Based on figure 4.20, the cooling associated with the evaporation of water corresponds to 20-30 % of the heat generated from the electrochemical reaction. The effects of evaporation become less significant at higher current densities since the heat from the chemical reactions increases both with the voltage and the current density.

4.7.1 Discussion of Implementation

Phase change in a porous media can be treated as a mass convection problem (Wu et al., 2009). The volume-specific mass flow rate due to phase change of water, Γ_{lg}, can then be modelled as stated in equation (4.9) (Olesen et al., 2019).

$$\Gamma_{\mathrm{lg}} = -a_{\mathrm{pm}} \varepsilon \alpha_{\mathrm{l}} \alpha_{\mathrm{g}} \frac{D_{\mathrm{H_2O,g}} Sh}{d_{\mathrm{pore}}} (p_{\mathrm{v}} - p_{\mathrm{sat}}) \tag{4.9}$$

Where a_{pm} is the interfacial area between the solid phase of the porous medium and the void space, $D_{\mathrm{H_2O,g}}$ is the mass diffusion coefficient of water vapour in the gas mixture, Sh is the Sherwood number, which represents the ratio of convective

mass transfer and diffusive mass transfer, d_{pore} is the characteristic pore diameter and ρ_{v} and ρ_{sat} is the vapor and saturation density.
The mass diffusion coefficient can be evaluated as stated in equation (4.10) (Wu et al., 2009).

$$D_{\mathrm{H_2O,O_2}} = D_{\mathrm{H_2O,O_2,0}} \frac{T}{T_0} \frac{p_0}{p} (\varepsilon(1-\alpha_{\mathrm{l}}))^{1.5} \tag{4.10}$$

Where $D_{\mathrm{H_2O,O_2,0}}$ is approximated as $D_{\mathrm{H_2O,air}}(T_0, p_0) = 2.5 \cdot 10^{-5}\ \mathrm{m^2/s}$, where $T_0 = 298$, $p_0 = 101$ kPa. The Sherwood number is the ratio of convective mass transfer to diffusive mass transfer and is evaluated in Wu et al. (2009) to be in the range of $2.04 \cdot 10^{-3} < Sh < 2.45 \cdot 10^{-1}$. The vapour and saturation density can be calculated as stated in equation (4.11) (Olesen et al., 2019).

$$\rho_{\mathrm{sat}} = \frac{p_{\mathrm{sat}}}{RT} \tag{4.11}$$

$$\rho_{\mathrm{v}} = \frac{x_{\mathrm{H_2O}} p_{\mathrm{g}}}{RT} \tag{4.12}$$

To model the mass diffusion due to concentration gradients, the conservation of species equation should also be introduced, which can be modelled in the following manner (Versteeg and Malalasekera, 2007):

$$\frac{\partial}{\partial t} \varepsilon \alpha_{\mathrm{g}} \rho_{\mathrm{g}} Y_{\mathrm{i}} + \nabla(\varepsilon \rho_{\mathrm{g}} \mathbf{u}_{\mathrm{g}} Y_{\mathrm{i}}) = \nabla(\varepsilon \alpha_{\mathrm{g}} [\rho_{\mathrm{g}} D^{eff}_{\mathrm{H_2O,O_2}} + \frac{\mu_{\mathrm{T,g}}}{Sc_{\mathrm{T,g}}}] \nabla Y_{\mathrm{i}}) + \dot{m}_{\mathrm{gl}} \tag{4.13}$$

Where Y_{i} is the mass fraction of species i, $\mu_{\mathrm{T,g}}$ and $Sc_{\mathrm{T,g}}$ is the turbulent dynamic viscosity and Schmidt number and $\dot{m}_{\mathrm{lg}}$ is the phase change mass flow rate. The Schmidt number presents the ratio of viscous diffusion to mass diffusion. The equation only needs to be introduced on the gas side, as the liquid phase is pure water.

Chapter 5

Recapitulation

5.1 Conclusion

This work presents the development of a multiphase solver in OpenFOAM suitable for describing the physical phenomena occurring in a PEMEC. The existing solvers lacked suitable porous treatment for multiphase flow when modelling the two-phase flow using the Euler-Euler approach. The study included an inspection of the effects of the porous layer, different flow regimes and the effects on the flow when including the lift force and heat transfer.

The solver was modified to include the generalised Darcy law and the capillary pressure in a defined porous region. The capillary pressure and the relative permeability were modelled using the van Genuchten model.

The inclusion of a porous layer increased the mixing of the liquid and gas flow. Increasing the permeability increased the mixing even further. Both the gas and liquid also had a higher velocity in the porous domain.

The standard conditions used for the simulation were a uniform current density of $i = 1\ \mathrm{A/cm^2}$ and a stoichiometric flow ratio of $\lambda = 350$. This resulted in the flow being in the stratified flow regime according to both the Mandhane flow map and the Taitel and Dukler flow map. Besides the stratified flow regime, the plug and slug flow regimes were also simulated. The stratified flow regime could be identified on inspection, but a VOF model is needed to clearly distinguish the other regimes.

The inclusion of lift and heat transfer only had minor effects on liquid and gas distribution. The temperature change from inlet to outlet was $\Delta T = 3.8$ K, which was well aligned with the analytically calculated temperature change of $\Delta T_{\text{analytical}} = 3.7$ K. In addition, an energy equation was solved for each phase, but the temperature difference between each phase was neglectable, meaning it could be considered to simplify the model by using a shared temperature field.

Phase change was not included in the model, but an analytical evaluation was done. The inclusion of phase change could have large effects on the flow, as, assuming the oxygen is fully humidified, the volume flow of water vapour corresponded to 38.5 % of the total flow at $\lambda = 350$. Heat transfer effects at $i = 1\ \text{A/cm}^2$ corresponded to 20 % of the heat released due to the overpotential, meaning heat transfer from phase change should also be considered.

5.2 Discussion and Future Work

The model developed in this paper was mainly developed based on the same modelling approaches seen in (Olesen et al., 2015) and (Olesen et al., 2019). The model was only tested on a simple geometry, and not validated against any data. For future work, the model would need validation, against either experimental data or existing models.

In the simple geometry considered, turbulence was not considered as the Reynolds number was low ($\mathcal{O}(10^2)$). In more advanced geometries, turbulence may become relevant. In OpenFOAM, existing turbulence models for multiphase flow however already exist. The effect of including a turbulence model could be considered for future work.

In Lenormand (1990) three different flow regimes were identified in the porous domain. In this project, the flow was identified to be somewhere between capillary fingering and viscous fingering. A different procedure for modelling the flow in the porous domain could therefore be considered. This could e.g. be based on the approach in Han et al. (2017) and Wang et al. (2022) where the velocity in the porous domain is modelled as a Darcy velocity and the contact angle is considered.

In OpenFOAM, the wall lubrication force is also available, but was not considered in this project. The wall lubrication force was originally proposed by Antal et al. (1991), in order to replicate bubble behaviour near walls found in experiments. However, the expected working flow regime is stratified and the wall lubrication force is mainly developed for bubbly flow and recommended to be turned off in flow regimes with higher void fractions (Lubchenko et al., 2018).

The developed model did not include phase change and as evaluated in section 4.7 on page 44, the total volume flow could consist of up to 38.5 % of the total volume flow and have a cooling effect of up to 20 % of the heat released due to the chemical reaction. The implementation was discussed in 4.7, but not implemented, as this would require larger implementations in the existing solvers in OpenFOAM. An initial simplified approach could be treating the water vapour as oxygen, meaning increasing the volume flow of oxygen and decreasing the fixed temperature gradient.

The current density was also considered uniform in this work. Future work could consider the implementation of an electrochemical model in order to simulate a non-uniform current density and determine the polarisation curve and the performance of the electrolyser.

Bibliography

ANSYS, 2013. ANSYS. *ANSYS Fluent Theory Guide 15*, 2013.

Antal et al., 1991. S P Antal, R T Lahey Jr and J E Flaherty. *ANALYSIS OF PHASE DISTRIBUTION IN FULLY DEVELOPED LAMINAR BUBBLY TWO-PHASE FLOW*, 1991.

A.P. Moller - Maersk and Lloyds Register, 10 2019. A.P. Moller - Maersk and Lloyds Register. *Alcohol, Biomethane and Ammonia are the best-positioned fuels to reach zero net emissions*, 2019. URL `https://tinyurl.com/yuptdps3`.

Araya et al., 2020. Samuel Simon Araya, Vincenzo Liso, Xiaoti Cui, Na Li, Jimin Zhu, Simon Lennart Sahlin, Søren Højgaard Jensen, Mads Pagh Nielsen and Søren Knudsen Kær. *A review of the methanol economy: The fuel cell route*. Energies, 13(3), 2020. ISSN 19961073. doi: 10.3390/en13030596.

Arbabi et al., 2016. F. Arbabi, H. Montazeri, R. Abouatallah, R. Wang and A. Bazylak. *Three-Dimensional Computational Fluid Dynamics Modelling of Oxygen Bubble Transport in Polymer Electrolyte Membrane Electrolyzer Porous Transport Layers*. Journal of The Electrochemical Society, 163(11), F3062–F3069, 2016. ISSN 0013-4651. doi: 10.1149/2.0091611jes.

Bachman, 2012. John Bachman. *Experimental investigation and optimization of polymer electrolyte membrane fuel cell parallel flow fields*, 2012. URL `https://www.researchgate.net/publication/277403689`.

Baker, 1954. Ovid Baker. *Design Of Pipelines For The Simultaneous Flow Of Oil And Gas*, Oil and Gas J., Dallas, Texas, 1954. URL `http://onepetro.org/SPEATCE/proceedings-pdf/53FM/All-53FM/SPE-323-G/2085003/spe-323-g.pdf/1`.

Bang, 2004. Mads Bang. *Modeling of Diffusive Convective and Electrochemical Processes in PEM fuel cells*, Institute of Energy Technology, Aalborg University, 2004.

Beale and Lehnert, 2021. Steven Beale and Werner Lehnert. *Lecture Notes in Energy: Electrochemical Cell Calculations with OpenFOAM*, volume 42. Springer Cham, 2021. URL `https://link.springer.com/bookseries/8874`.

Beale et al., 3 2016. Steven B. Beale, Hae Won Choi, Jon G. Pharoah, Helmut K. Roth, Hrvoje Jasak and Dong Hyup Jeon. *Open-source computational model of a solid oxide fuel cell*. Computer Physics Communications, 200, 15–26, 2016. ISSN 00104655. doi: 10.1016/j.cpc.2015.10.007.

Berning and Al Shakhshir, 3 2016. Torsten Berning and Saher Al Shakhshir. *Applying hot-wire anemometry to directly measure the water balance in a proton exchange membrane fuel cell for a pre-humidified hydrogen stream*. International Journal of Hydrogen Energy, 41(10), 5315–5320, 2016. ISSN 03603199. doi: 10.1016/j.ijhydene.2016.01.136.

Bessarabov et al., 2015. Dmitri Bessarabov, Haijiang Wang, Hui Li and Nana Zhao. *PEM Electrolysis for Hydrogen Production*. CRC Press, Boca Raton, 2015. ISBN 9781482252293. doi: 10.1201/b19096.

Burns et al., 2004. Alan D Burns, Thomas Frank, Ian Hamill and Jun-Mei Shi. *The Favre Averaged Drag Model for Turbulent Dispersion in Eulerian Multi-Phase Flows*, 2004.

Busch, 2015. Sandra Busch. *CFD with OpenSource software: A twophaseEulerFoam tutorial*, Chalmers University of Technology, 2015.

Carmo et al., 4 2013. Marcelo Carmo, David L. Fritz, Jürgen Mergel and Detlef Stolten. *A comprehensive review on PEM water electrolysis*, 2013. ISSN 03603199, In *International Journal of Hydrogen Energy*.

Carrillo and Bourg, 10 2019. Francisco J. Carrillo and Ian C. Bourg. *A Darcy-Brinkman-Biot Approach to Modeling the Hydrology and Mechanics of Porous Media Containing Macropores and Deformable Microporous Regions*. Water Resources Research, 55(10), 8096–8121, 2019. ISSN 19447973. doi: 10.1029/2019WR024712.

Carrillo and Bourg, 2 2021. Francisco J. Carrillo and Ian C. Bourg. *Modeling Multiphase Flow Within and Around Deformable Porous Materials: A Darcy-Brinkman-Biot Approach*. Water Resources Research, 57(2), 2021. ISSN 19447973. doi: 10.1029/2020WR028734.

Carrillo et al., 9 2020. Francisco J. Carrillo, Ian C. Bourg and Cyprien Soulaine. *Multiphase flow modeling in multiscale porous media: An open-source micro-continuum approach*. Journal of Computational Physics: X, 8, 2020. ISSN 25900552. doi: 10.1016/j.jcpx.2020.100073.

Celik et al., 7 2008. Ismail B. Celik, Urmila Ghia, Patrick J. Roache, Christopher J. Freitas, Hugh Coleman and Peter E. Raad. *Procedure for estimation and reporting of uncertainty due to discretization in CFD applications*. Journal of Fluids Engineering, Transactions of the ASME, 130(7), 0780011–0780014, 2008. ISSN 00982202. doi: 10.1115/1.2960953/444689. URL `http://asmedigitalcollection.asme.org/fluidsengineering/article-pdf/130/7/078001/5491455/078001_1.pdf`.

Crowe, 2006. Clayton Crowe. *Multiphase Flow Handbook*. Taylor & Francis Group, 2006.

EU, 2021. EU. *Europe's 2030 climate and energy targets : research & innovation actions*, European Commission, Directorate-General for Research and Innovation, 2021.

Franc et al., 2016. Jacques Franc, Pierre Horgue, Romain Guibert and Gerald Debenest. *Benchmark of different CFL conditions for IMPES*, 2016.

Gostick et al., 6 2006. Jeffrey T. Gostick, Michael W. Fowler, Marios A. Ioannidis, Mark D. Pritzker, Y. M. Volfkovich and A. Sakars. *Capillary pressure and hydrophilic porosity in gas diffusion layers for polymer electrolyte fuel cells*. Journal of Power Sources, 156(2), 375–387, 2006. ISSN 03787753. doi: 10.1016/J.JPOWSOUR.2005.05.086.

Greenshields and Weller, 2022. C. Greenshields and H. Weller. *Notes on Computational Fluid Dynamics: General Principles*. CFD Direct Ltd, 2022. ISBN 978-1-3999-2078-0. URL `https://doc.cfd.direct/notes/cfd-general-principles/index/`.

Greenshields, 2022. Christopher Greenshields. *OpenFOAM v10 User Guide*. The OpenFOAM Foundation, 2022. URL `https://doc.cfd.direct/openfoam/user-guide-v10/`.

Grigoriev et al., 10 2020. S. A. Grigoriev, V. N. Fateev, D. G. Bessarabov and P. Millet. *Current status, research trends, and challenges in water electrolysis science and technology*. International Journal of Hydrogen Energy, 45(49), 26036–26058, 2020. ISSN 03603199. doi: 10.1016/j.ijhydene.2020.03.109.

Guerrero et al., 2017. Esteban Guerrero, Felipe Muñoz and Nicolás Ratkovich. *COMPARISON BETWEEN EULERIAN AND VOF MODELS FOR TWO-PHASE FLOW ASSESSMENT IN VERTICAL PIPES COMPARISON BETWEEN EULERIAN AND VOF MODELS FOR TWO-PHASE FLOW ASSESSMENT IN VERTICAL PIPES RESUMEN RESUMO COMPARISON BETWEEN EULERIAN AND VOF MODELS FOR TWO-PHASE FLOW ASSESSMENT IN VERTICAL PIPES*. Tecnología y Futuro, 7, 2017. ISSN 2382-4581.

Hærvig, 2017. Jakob Hærvig. *On the Adhesive Behaviour of Micron-Sized Particle in Turbulent Flow*, Aalborg University, 2017. URL `https://doi.org/10.5278/vbn.phd.eng.00022`.

Han et al., 2 2017. Bo Han, Jingke Mo, Zhenye Kang, Gaoqiang Yang, William Barnhill and Feng Yuan Zhang. *Modeling of two-phase transport in proton exchange membrane electrolyzer cells for hydrogen energy*. International Journal of Hydrogen Energy, 42(7), 4478–4489, 2017. ISSN 03603199. doi: 10.1016/j.ijhydene.2016.12.103.

HONDA, 2019. HONDA. *Smart Hydrogen Station*, 2019.

Horgue et al., 2014. P Horgue, C Soulaine, J Franc, R Guibert and G Debenest. *An open-source toolbox for multiphase flow in porous media*, 2014.

Horgue et al., 2015. Pierre Horgue, Jacques Franc, Romain Guibert and Gérald Debenest. *An extension of the open-source porousMultiphaseFoam toolbox dedicated to groundwater flows solving the Richards' equation*, 2015.

IEA, 2019. IEA. *The Future of Hydrogen*, 2019.

Ishii and Zuber, 1979. Mamoru Ishii and Novak Zuber. *Drag coefficient and relative velocity in bubbly, droplet or particulate flows*. AIChE Journal, 25(5), 843–855, 1979. ISSN 15475905. doi: 10.1002/aic.690250513.

Lafmejani et al., 6 2017. Saeed Sadeghi Lafmejani, Anders Christian Olesen and Søren Knudsen Kær. *VOF modelling of gas–liquid flow in PEM water electrolysis cell micro-channels*. International Journal of Hydrogen Energy, 42(26), 16333–16344, 2017. ISSN 03603199. doi: 10.1016/j.ijhydene.2017.05.079.

Lenormand, 1990. R Lenormand. *Liquids in porous media*, 1990.

Lubchenko et al., 1 2018. Nazar Lubchenko, Ben Magolan, Rosie Sugrue and Emilio Baglietto. *A more fundamental wall lubrication force from turbulent dispersion regularization for multiphase CFD applications*. International Journal of Multiphase Flow, 98, 36–44, 2018. ISSN 03019322. doi: 10.1016/j.ijmultiphaseflow.2017.09.003.

Lumen, 2023. Lumen. *Reading: Porosity and Permeability*, 2023. URL `Reading:PorosityandPermeability`.

Mandhane et al., 1974. J M Mandhane, G A Gregory and K Aziz. *A FLOW PATTERN MAP FOR GAS-LIQUID FLOW IN HORIZONTAL PIPES*, 1974.

Manni, 2014. Alessandro Manni. *CFD with OpenSource software: An introduction to twoPhaseEulerFoam with addition of an heat exchange model*, Chalmers University of Technology, 2014.

Muskat et al., 2 1937. M Muskat, R D Wyckoff, H G Botset and M W Meres'. *Chapter II. Production Engineering Research: Flow of Gas-liquid Mixtures through Sands*, New York Meeting, 2 1937. URL `http://onepetro.org/TRANS/article-pdf/123/01/69/2178346/spe-937069-g.pdf/1`.

Nam and Kaviany, 2003. Jin Hyun Nam and Massoud Kaviany. *Effective diffusivity and water-saturation distribution in single- and two-layer PEMFC diffusion medium*. International Journal of Heat and Mass Transfer, 46(24), 4595–4611, 2003. ISSN 00179310. doi: 10.1016/S0017-9310(03)00305-3.

Norouzi, 2020. Hamidreza Norouzi. *Mastering twoPhaseEulerFoam Three: Bubble Column*, Center of Engineering and Multiscale Modeling of Fluid Flow, 2020.

O'Hayre et al., 5 2016. Ryan O'Hayre, Suk-Won Cha, Whitney Colella and Fritz B. Prinz. *Fuel Cell Fundamentals*. Fuel Cell Fundamentals, 2016. doi: 10.1002/9781119191766. URL `https://onlinelibrary.wiley.com/doi/book/10.1002/9781119191766`.

Olesen et al., 2015. Anders Christian Olesen, Carsten Rømer and Søren Knudsen Kær. *A numerical study of the gas-liquid, two-phase flow maldistribution in the anode of a high pressure PEM water electrolysis cell*. International Journal of Hydrogen Energy, (41), 52–68, 2015.

Olesen et al., 1 2019. Anders Christian Olesen, Steffen Henrik Frensch and Søren Knudsen Kær. *Towards uniformly distributed heat, mass and charge: A flow field design study for high pressure and high current density operation of PEM electrolysis cells*. Electrochimica Acta, 293, 476–495, 2019. ISSN 00134686. doi: 10.1016/j.electacta.2018.10.008.

Olesen et al., 10 2022. Anders Christian Olesen, Søren Knudsen Kær and Torsten Berning. *A Multi-Fluid Model for Water and Methanol Transport in a Direct Methanol Fuel Cell*. Energies, 15(19), 2022. ISSN 19961073. doi: 10.3390/en15196869.

Otromke, 2013. Malte Otromke. *Implementation and Comparison of Correlations for interfacial Forces in a Gas-Liquid System within an Euler-Euler Framework*, 2013.

Rasul et al., 7 2020. Golam Rasul, M. Fahed Qureshi, Hicham Ferroudji, Stephen Butt, Rashid Hasan, Ibrahim Hassan and Mohammad Azizur Rahman. *Analysis of cuttings transport and flow pattern in nearly horizontal extended reach well*. Journal of Advanced Research in Fluid Mechanics and Thermal Sciences, 71(2), 69–86, 2020. ISSN 22897879. doi: 10.37934/arfmts.71.2.6986.

Rho et al., **12 2020**. Kyu Heon Rho, Youngseung Na, Taewook Ha and Dong Kyu Kim. *Performance analysis of polymer electrolyte membrane water electrolyzer using openfoam®: Two-phase flow regime, electrochemical model*. Membranes, 10(12), 1–15, 2020. ISSN 20770375. doi: 10.3390/membranes10120441.

Schmidt et al., **12 2017**. O. Schmidt, A. Gambhir, I. Staffell, A. Hawkes, J. Nelson and S. Few. *Future cost and performance of water electrolysis: An expert elicitation study*. International Journal of Hydrogen Energy, 42(52), 30470–30492, 2017. ISSN 03603199. doi: 10.1016/j.ijhydene.2017.10.045.

Shiva Kumar and Himabindu, **12 2019**. S. Shiva Kumar and V. Himabindu. *Hydrogen production by PEM water electrolysis – A review*, 2019. ISSN 25892991, In *Materials Science for Energy Technologies*.

Sinha and Wang, **11 2007**. Puneet K. Sinha and Chao Yang Wang. *Pore-network modeling of liquid water transport in gas diffusion layer of a polymer electrolyte fuel cell*. Electrochimica Acta, 52(28), 7936–7945, 2007. ISSN 00134686. doi: 10.1016/j.electacta.2007.06.061.

Taitel and Dukler, **1976**. Yemada Taitel and A. E. Dukler. *A model for predicting flow regime transitions in horizontal and near horizontal gas-liquid flow*. AIChE journal, 22(1), 47–55, 1976. ISSN 0001-1541. doi: 10.1002/aic.690220105.

UNFCCC, *2015*. UNFCCC. Adoption of the Paris Agreement. In *21st Conference of the Parties*. United Nations / Framework Convention on Climate Change, 2015.

Versteeg and Malalasekera, **2007**. H K. Versteeg and W. Malalasekera. *An Introduction to COMPUTATIONAL FLUID DYNAMICS The Finite Volume Method*. Pearson Education Limited, 2. ed. edition, 2007. ISBN 978-0-13-127498-3.

Wang et al., **5 2022**. Xue Ye Wang, Zhi Ming Wang, Yuan Cheng Feng, Chao Xu, Zhi Chao Chen, Zhi Rong Liao and Xing Ju. *Three-dimensional multiphase modeling of a proton exchange membrane electrolysis cell with a new interdigitated-jet hole flow field*. Science China Technological Sciences, 65(5), 1179–1192, 2022. ISSN 18691900. doi: 10.1007/s11431-022-2026-6.

Wu et al., **11 2009**. Hao Wu, Xianguo Li and Peter Berg. *On the modeling of water transport in polymer electrolyte membrane fuel cells*. Electrochimica Acta, 54(27), 6913–6927, 2009. ISSN 00134686. doi: 10.1016/j.electacta.2009.06.070.

Appendix A

Solver Settings and Schemes

This appendix will briefly explain the different solvers applied and numerical schemes.

The transient PIMPLE algorithm is used to couple the pressure and velocity, and is a combination of the PISO and SIMPLE algorithms. The PISO is a transient solver, using 3rd-order accurate relations for the pressure and 4th-order accurate for the velocity. The SIMPLE algorithm is only a steady-state solution in OpenFOAM and uses an iterative process to find a solution. PIMPLE combines the two algorithms, using a PISO algorithm in the inner loop and a SIMPLE in the outer loop, with a defined number of iterations (Greenshields and Weller, 2022). In this case, two iterations are used in the inner loop and three iterations in the outer loop.

The timestep used is limited by a maximum Courant number of $Co_{\mathrm{max}} = 0.9$. The Courant number in OpenFOAM is defined as:

$$Co_{\mathrm{i}} = \frac{\Delta t}{2V_{\mathrm{i}}} \sum_{\mathrm{j} \in faces} \left| \mathbf{u}_{\mathrm{i}} \cdot \mathbf{n}_{\mathrm{i,j}} A_{\mathrm{i,j}} \right| \tag{A.1}$$

For the discretisation of the governing equations, the following numerical schemes have been applied:

$$\underbrace{\frac{\partial}{\partial t}(\varepsilon \alpha_{\mathrm{i}} \rho_{i})}_{Euler} + \underbrace{\nabla(\varepsilon \alpha_{\mathrm{i}} \rho_{\mathrm{i}} \mathbf{u}_{\mathrm{i}})}_{Limitedlinear} = 0 \tag{A.2}$$

$$\underbrace{\frac{\partial}{\partial t} \varepsilon \alpha_{\mathrm{i}} \rho_{\mathrm{i}} \mathbf{u}_{\mathrm{i}}}_{Euler} + \underbrace{\nabla(\varepsilon \alpha_{\mathrm{i}} \rho_{\mathrm{i}} \mathbf{u}_{\mathrm{i}} \mathbf{u}_{\mathrm{i}})}_{Limitedlinear} = \varepsilon \alpha_{\mathrm{i}} \rho_{\mathrm{i}} \mathbf{g} - \underbrace{\varepsilon \alpha_{\mathrm{i}} \nabla p_{\mathrm{l}}}_{Limitedlinear} - \underbrace{\varepsilon \alpha_{\mathrm{i}} \nabla \tau_{\mathrm{i}}}_{Linear} + \varepsilon \alpha_{\mathrm{i}} M_{\mathrm{i}} \tag{A.3}$$

A short description of the relevant schemes is given in the list below, based on the description given in Greenshields and Weller (2022) and Greenshields (2022).

- **Euler** is a bounded, transient scheme. It is first order accurate and assumed to be sufficiently accurate, as the time step is limited by $Co_{\text{max}} < 0.9$ and three outer corrections are used.
- **Gauss linear** is a unbounded second order scheme.
- **Gauss limited linear**, this scheme uses linear towards upwind, making it more stable than linear, but less accurate.
- **Gauss upwind** is the most stable scheme and is bounded, conservative and transportiveness is built into the formulation, but is only 1st order accurate.

Appendix B

Grid Independent Study

Three different grids of 49, 110 and 208 thousand cells are generated, illustrated on figure B.1.

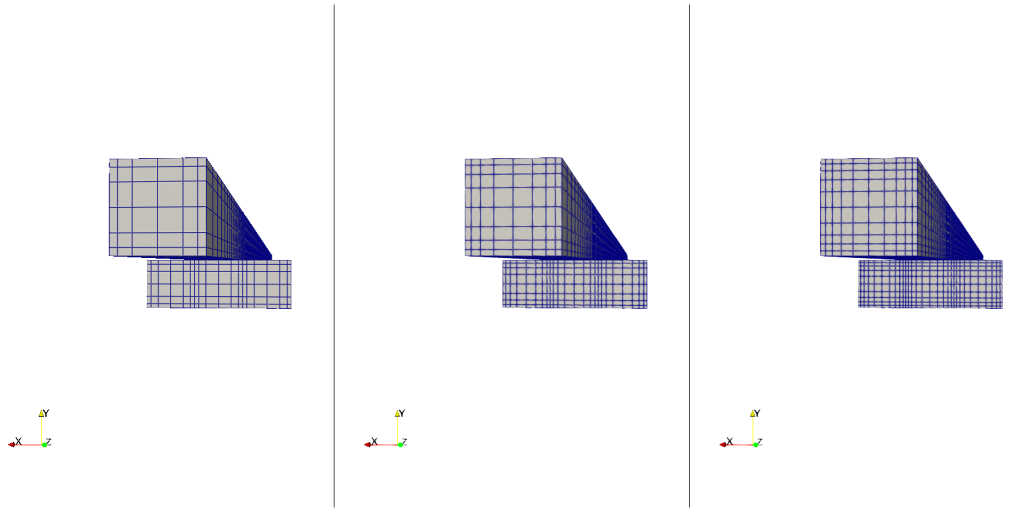

Figure B.1: The three different meshes. From left to right, mesh 1, 2 and 3, of 49, 110 and 208 thousand cells respectively.

The parameters inspected for a grid-independent study are the phase volume fraction, velocity of each phase, and pressure distribution. To compare the difference in the results of the used grids, data is taken from a slice in the x-plane in the middle of the PEMEC, in the z-plane at the entrance to the outlet region and at the outlet. The regions are illustrated on figure B.2.

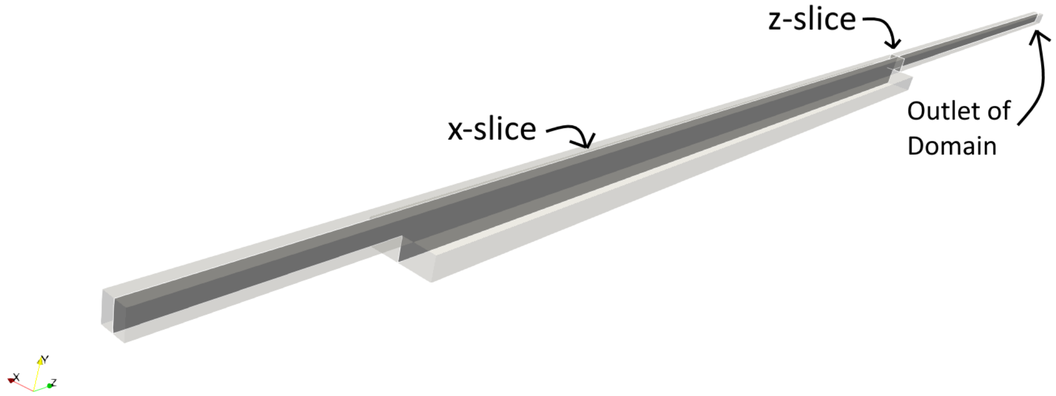

Figure B.2: Regions for the grid independent study.

The data used is time-averaged over a 7-second period, after an initial 1-second period as well as using interpolated data from an initial coarser mesh. At the z-slice and outlet, the data is area averaged, and the grid convergence index (GCI) method is used, as introduced in appendix C. The results of the study are illustrated on figure B.3.

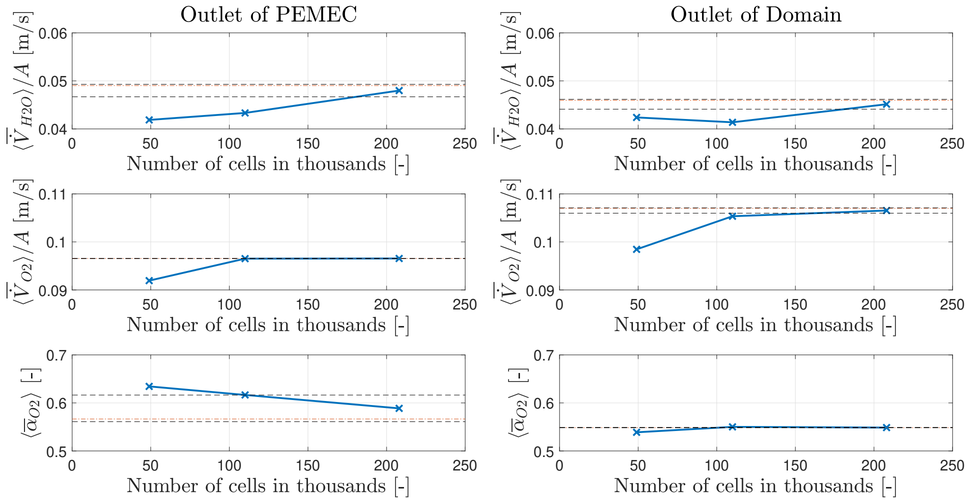

Figure B.3: Area and time-averaged values at the z-slice at the outlet of the PEMEC on the left and the outlet of the domain on the right. From top to bottom, is $\langle\overline{\dot{V}_{\mathrm{H2O}}}\rangle/A$, $\langle\overline{\dot{V}_{\mathrm{O2}}}\rangle/A$ and $\langle\overline{\alpha_{\mathrm{O_2}}}\rangle$. The black dashed lines are the error bands of the finest mesh, estimated using the GCI method. The red dashed-dotted line is the extrapolated value using the GCI method.

Where $\langle\overline{\dot{V}_{\mathrm{i}}}\rangle/A$ is the time-averaged volumetric flux of H_2O and O_2 respectively, given by $\langle\overline{\dot{V}_{\mathrm{i}}}\rangle/A = (\int(\langle\alpha_{\mathrm{i}}u_{\mathrm{i}}\rangle)dA)/A$. Table B.1 gives an overview of the estimated errors.

Parameter	Estimated Error, Mesh 3 Outlet of PEMEC	Estimated Error, Mesh 3 Outlet of Domain
$\langle\overline{\dot{V}_{\mathrm{H_2O}}}\rangle/A$	2.7 %	2.3 %
$\langle\overline{\dot{V}_{\mathrm{O_2}}}\rangle/A$	$8.7\cdot10^{-4}$ %	$5.2\cdot10^{-1}$ %
$\langle\overline{\alpha_{\mathrm{O_2}}}\rangle$	4.7 %	$8.0\cdot10^{-2}$ %
$\langle\overline{p}\rangle$	0	0

Table B.1: Overview of estimated errors of mesh 3, based on the GCI method. *Note that the GCI method can become inaccurate when the difference is close to 0.

At the x-slice in the middle of PEMEC, a visual comparison is done. The figures B.4, B.5, B.6 and B.7 illustrates $\langle\alpha_{\mathrm{O_2}}\rangle$, $\langle p\rangle$, $\langle u_{\mathrm{H_2O}}\rangle$ and $\langle u_{\mathrm{O_2}}\rangle$.

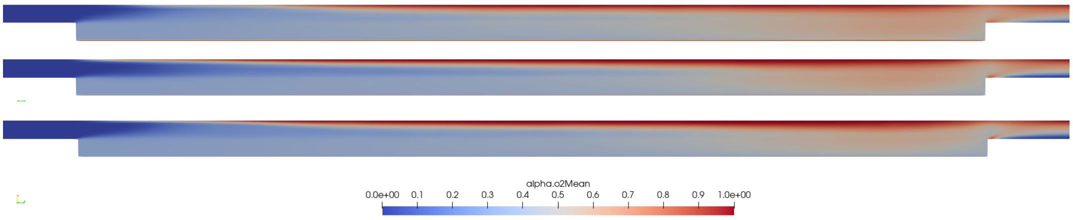

Figure B.4: Time averaged $\langle\alpha_{\mathrm{O_2}}\rangle$ for the three meshes. From the top down is the mesh of 49, 110 and 208 thousand cells.

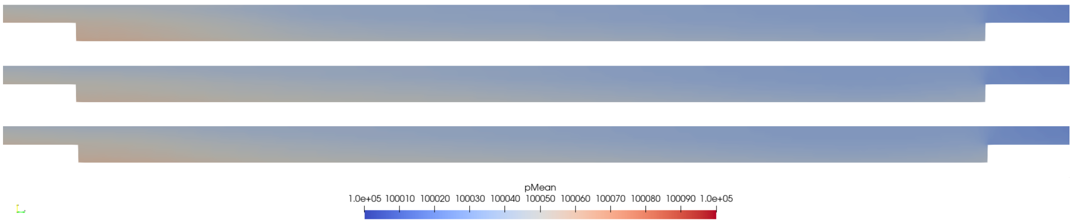

Figure B.5: Time averaged $\langle p\rangle$ for the three meshes. From the top down is the mesh of 49, 110 and 208 thousand cells.

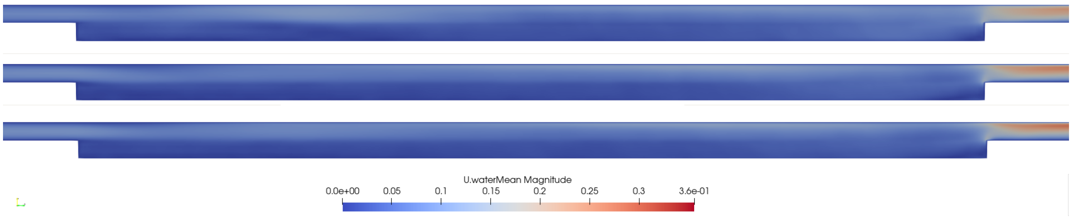

Figure B.6: Time averaged $\langle u_{H_2O} \rangle$ for the three meshes. From the top down is the mesh of 49, 110 and 208 thousand cells.

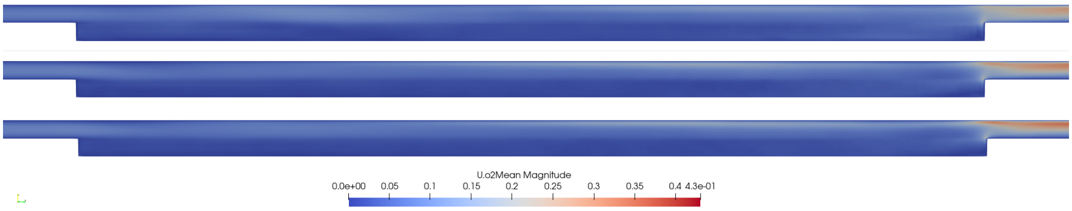

Figure B.7: Time averaged $\langle u_{O_2} \rangle$ for the three meshes. From the top down is the mesh of 49, 110 and 208 thousand cells.

Based on the visual comparison and the estimated errors based on the GCI method, the third mesh is assumed to be sufficiently accurate.

Appendix C

Grid Convergence Index Method

The GCI method is executed as recommended in Celik et al. (2008).

The first step of the GCI method is to define three meshes. The next step is to define a refinement factor r_{ij} (C.1).

$$r_{\mathrm{cm}} = \frac{N_{\mathrm{m}}^{1/3}}{N_{\mathrm{c}}^{1/3}} \quad r_{\mathrm{mf}} = \frac{N_{\mathrm{f}}^{1/3}}{N_{\mathrm{m}}^{1/3}} \tag{C.1}$$

The refinement factor should preferably be >1.3. Then the solution difference ϵ_{ij} is determined (C.2).

$$\epsilon_{\mathrm{cm}} = \phi_{\mathrm{c}} - \phi_{\mathrm{m}} \quad \epsilon_{\mathrm{mf}} = \phi_{\mathrm{m}} - \phi_{\mathrm{f}} \tag{C.2}$$

The next step is to calculate the apparent order P (C.3), using fixed point iteration.

$$P = \frac{1}{\ln(r_{\mathrm{mf}})} \left| \ln \left| \frac{\varepsilon_{\mathrm{cm}}}{\varepsilon_{\mathrm{mf}}} \right| + \ln \left(\frac{r_{\mathrm{mf}}^{P} - s}{r_{\mathrm{cm}}^{P} - s} \right) \right| \qquad s = \mathrm{sign}\left(\frac{\varepsilon_{\mathrm{cm}}}{\varepsilon_{\mathrm{mf}}} \right) \tag{C.3}$$

The extrapolated value $\phi_{\mathrm{mf}}^{(ext)}$ is determined using equation (C.4).

$$\phi_{mf}^{(ext)} = \frac{r_{\mathrm{mf}}^{P} \phi_{f} - \phi_{\mathrm{m}}}{r_{\mathrm{mf}}^{P} - 1} \tag{C.4}$$

The approximate, $e_{\mathrm{mf}}^{(a)}$, and extrapolated error, e_{mf}^{ext}, can then be calculated using equation (C.5), and the GCI_{f} for the fine mesh is determined using equation (C.6).

$$e_{\mathrm{mf}}^{(a)} = \left| \frac{\phi_{\mathrm{f}} - \phi_{\mathrm{m}}}{\phi_{\mathrm{f}}} \right| \quad e_{mf}^{ext} = \left| \frac{\phi_{\mathrm{mf}}^{(ext)} - \phi_{\mathrm{m}}}{\phi_{\mathrm{mf}}^{(ext)}} \right| \tag{C.5}$$

$$GCI_{\mathrm{f}} = \frac{1.25 e_{\mathrm{mf}}^{(a)}}{r_{\mathrm{mf}}^{P} - 1} \tag{C.6}$$

Appendix D

Taitel and Dukler Flow Pattern Map

The Taitel and Dukler map is a complex flow pattern map proposed in Taitel and Dukler (1976). The flow map requires the evaluation of the following dimensionless parameters:

$$X = \left[\frac{(dp/dz)_\mathrm{l}}{(dp/dz)_\mathrm{g}}\right]^{1/2} \tag{D.1}$$

$$Fr = \frac{G_\mathrm{g}}{[\rho_\mathrm{g}(\rho_\mathrm{l} - \rho_\mathrm{g}) D_\mathrm{h} g]^{1/2}} \tag{D.2}$$

$$T = \left[\frac{|(dp/dz)_\mathrm{l}|}{g(\rho_\mathrm{l} - \rho_\mathrm{g})}\right] \tag{D.3}$$

$$K = Fr\left(\frac{G_\mathrm{l} D_\mathrm{h}}{\mu_\mathrm{l}}\right) \tag{D.4}$$

Where X is the Martinelli parameter and Fr is the Froude number, T and K are specific constants for the Taitel and Dukler map, G_i is the mass flux of phase i and D_h is the hydraulic diameter.

The pressure drops $(dp/dz)_\mathrm{i}$ for each phase are evaluated using the following equation:

$$(dp/dz)_\mathrm{l} = \frac{4c_\mathrm{l}}{D_\mathrm{h}}\left(\frac{V_\mathrm{l} D_\mathrm{h}}{\nu_\mathrm{l}}\right)^{-n}\frac{\rho_\mathrm{l} V_\mathrm{l}^2}{2} \quad (dp/dz)_\mathrm{g} = \frac{4c_\mathrm{g}}{D_\mathrm{h}}\left(\frac{V_\mathrm{g} D_\mathrm{h}}{\nu_\mathrm{g}}\right)^{-m}\frac{\rho_\mathrm{g} V_\mathrm{g}^2}{2} \tag{D.5}$$

Where V_i is the superficial velocity of phase i and the parameters n, m, c_i are constants depending on whether the flow is turbulent or laminar and have the following correlation:

$$c_{\mathrm{i}} = \begin{cases} 0.046, & \text{Turbulent} \\ 16, & \text{Laminar} \end{cases} \tag{D.6}$$

$$m = \begin{cases} 0.2, & \text{Turbulent, gas} \\ 1, & \text{Laminar, gas} \end{cases} \qquad n = \begin{cases} 0.2, & \text{Turbulent, liquid} \\ 1, & \text{Laminar, liquid} \end{cases} \tag{D.7}$$

Figure D.1 illustrates the evaluated flow regimes.

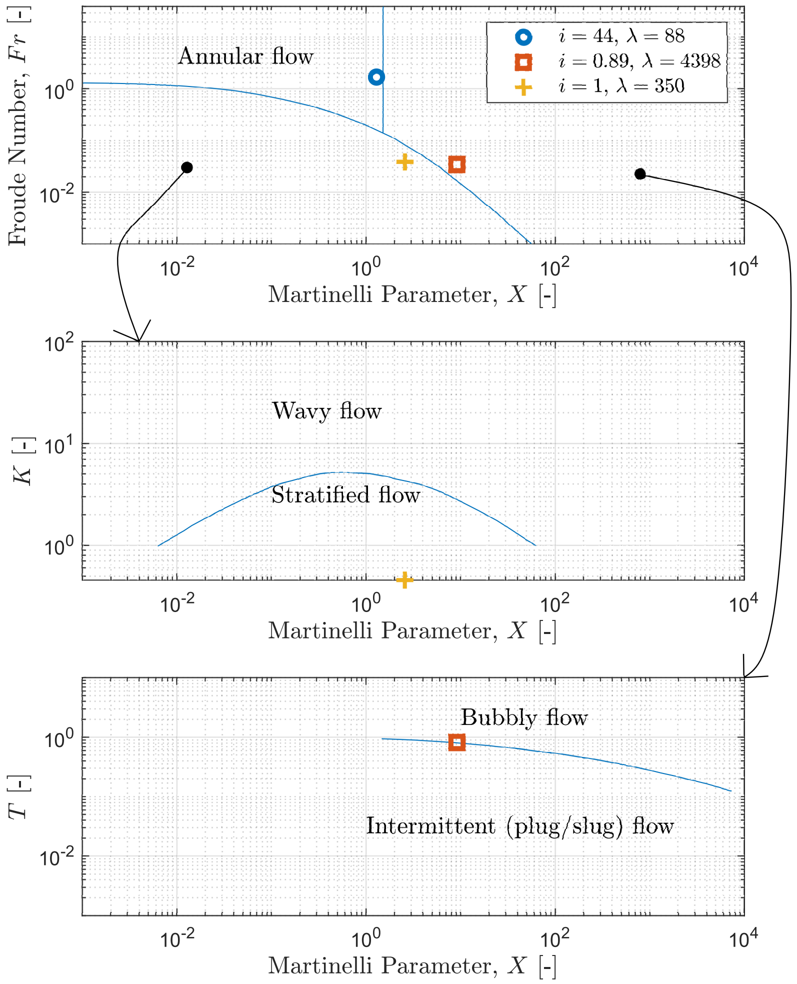

Figure D.1: Taitel and Dukler complex flow map. Based on Taitel and Dukler (1976). The points marked are the points analysed in 4.4 on page 35.

Appendix E

Flow Regime Results

In this appendix, additional results from section 4.4 on page 35 is illustrated. A quick overview of what each figure illustrates is given in the table E.1

Figure	Parameter	Region	Figure	Parameter	Region
E.1	p	PEMEC	E.2	p	Outlet
E.3	u_{O_2}	PEMEC	E.4	u_{O_2}	Outlet
E.5	u_{H_2O}	PEMEC	E.6	u_{H_2O}	Outlet
E.7	p	PEMEC	E.8	p	Outlet
E.9	u_{O_2}	PEMEC	E.10	u_{O_2}	Outlet
E.11	u_{H_2O}	PEMEC	E.12	u_{H_2O}	Outlet
E.13	p	PEMEC	E.14	p	Outlet
E.15	u_{O_2}	PEMEC	E.16	u_{O_2}	Outlet
E.17	u_{H_2O}	PEMEC	E.18	u_{H_2O}	Outlet

Table E.1: Overview of parameters illustrates by the figures and in what region.

E.1 Stratified flow

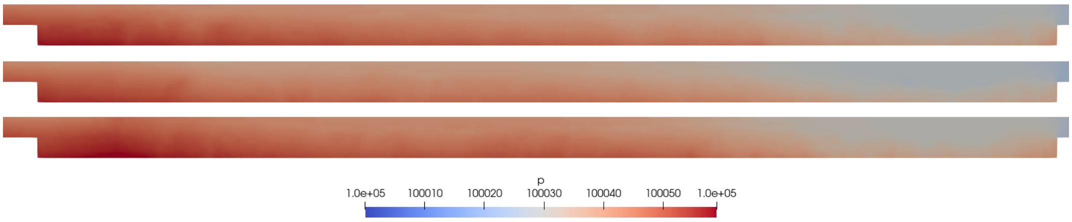

Figure E.1: The transient flow in the PEMEC, for the stratified flow. From top to bottom is the flow at the minimum, mid and maximum point. The parameter illustrated is p.

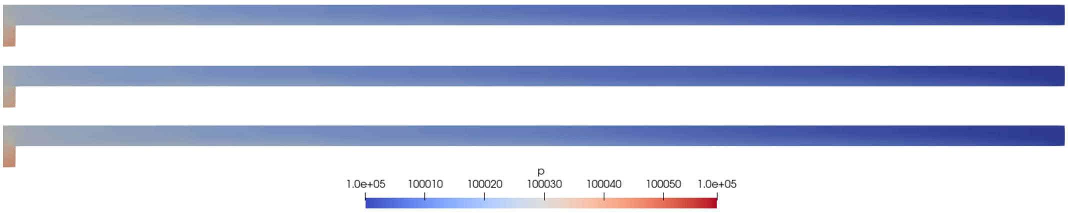

Figure E.2: The transient flow at the outlet, for the stratified flow. From top to bottom is the flow at the minimum, mid and maximum point. The parameter illustrated is p.

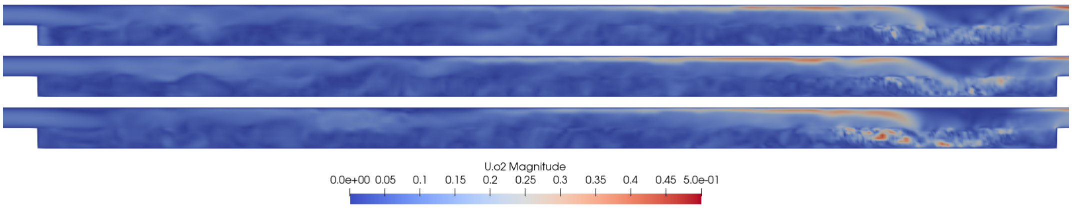

Figure E.3: The transient flow in the PEMEC, for the stratified flow. From top to bottom is the flow at the minimum, mid and maximum point. The parameter illustrated is u_{O_2}.

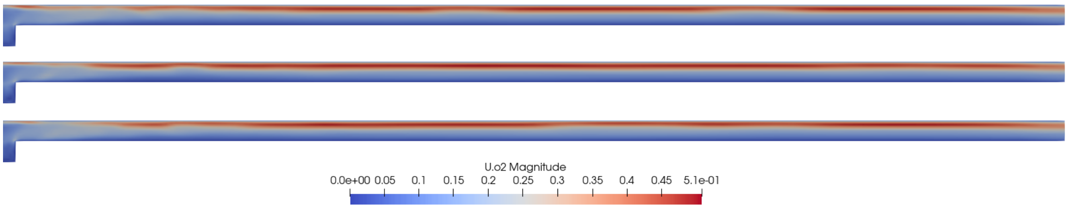

Figure E.4: The transient flow at the outlet, for the stratified flow. From top to bottom is the flow at the minimum, mid and maximum point. The parameter illustrated is u_{O_2}.

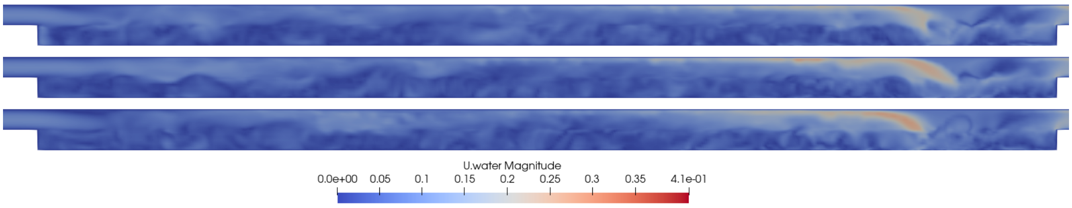

Figure E.5: The transient flow in the PEMEC, for the stratified flow. From top to bottom is the flow at the minimum, mid and maximum point. The parameter illustrated is u_{H_2O}.

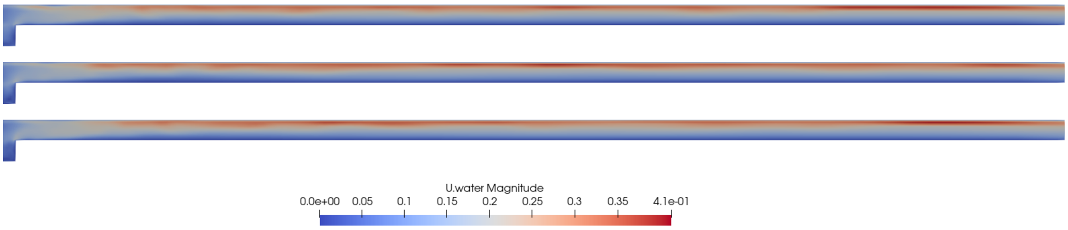

Figure E.6: The transient flow at the outlet, for the stratified flow. From top to bottom is the flow at the minimum, mid and maximum point. The parameter illustrated is u_{H_2O}.

E.2 Plug flow

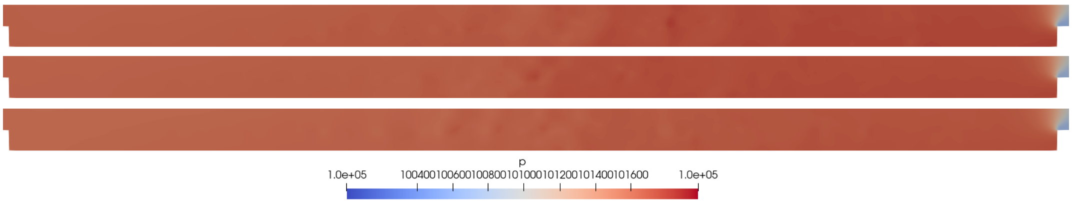

Figure E.7: The transient flow in the PEMEC, for the plug flow. From top to bottom is the flow at the minimum, mid and maximum point. The parameter illustrated is p.

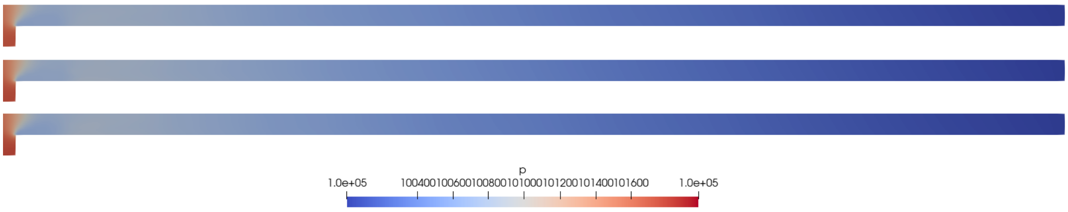

Figure E.8: The transient flow at the outlet, for the plug flow. From top to bottom is the flow at the minimum, mid and maximum point. The parameter illustrated is p.

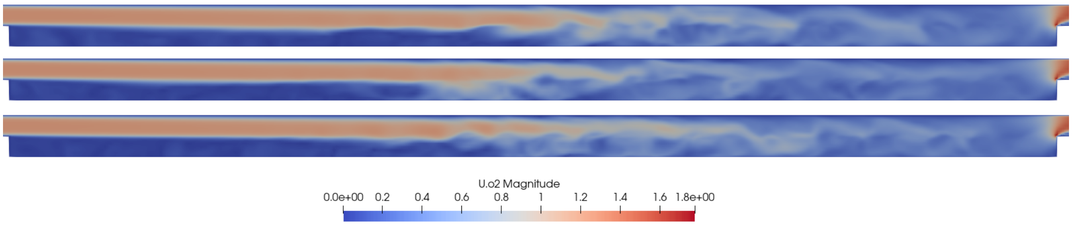

Figure E.9: The transient flow in the PEMEC, for the plug flow. From top to bottom is the flow at the minimum, mid and maximum point. The parameter illustrated is u_{O_2}.

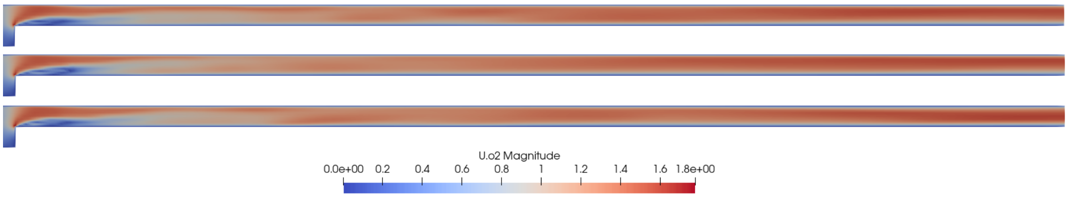

Figure E.10: The transient flow at the outlet, for the plug flow. From top to bottom is the flow at the minimum, mid and maximum point. The parameter illustrated is u_{O_2}.

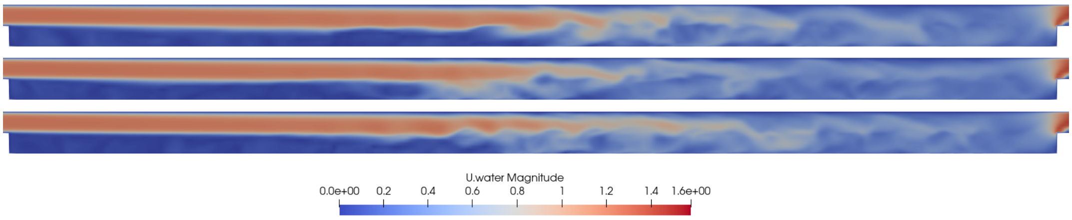

Figure E.11: The transient flow in the PEMEC, for the plug flow. From top to bottom is the flow at the minimum, mid and maximum point. The parameter illustrated is u_{H_2O}.

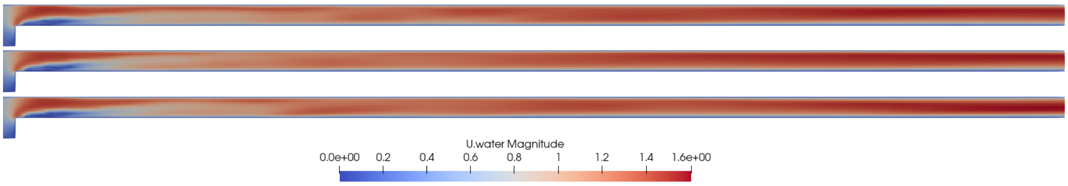

Figure E.12: The transient flow at the outlet, for the plug flow. From top to bottom is the flow at the minimum, mid and maximum point. The parameter illustrated is u_{H_2O}.

E.3 Slug flow

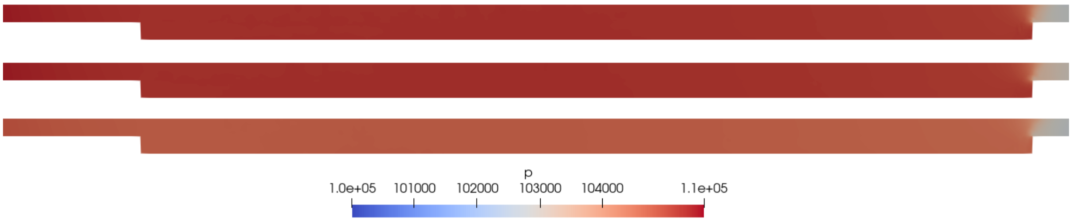

Figure E.13: The transient flow in the PEMEC, for the slug flow. From top to bottom is the flow at the minimum, mid and maximum point. The parameter illustrated is p.

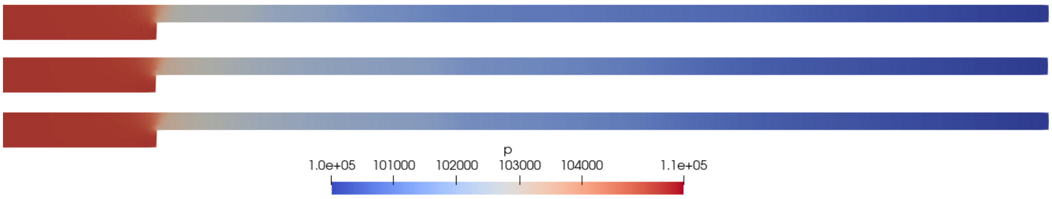

Figure E.14: The transient flow at the outlet, for the slug flow. From top to bottom is the flow at the minimum, mid and maximum point. The parameter illustrated is p.

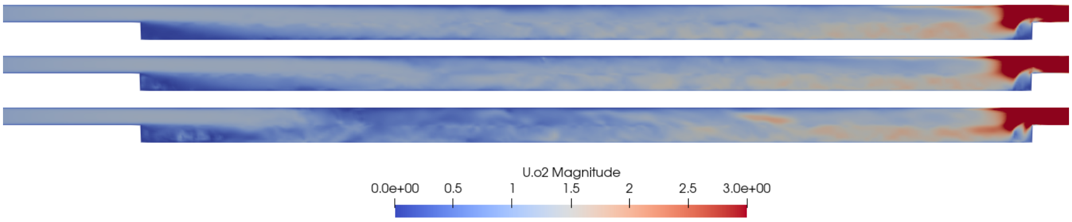

Figure E.15: The transient flow in the PEMEC, for the slug flow. From top to bottom is the flow at the minimum, mid and maximum point. The parameter illustrated is u_{O_2}.

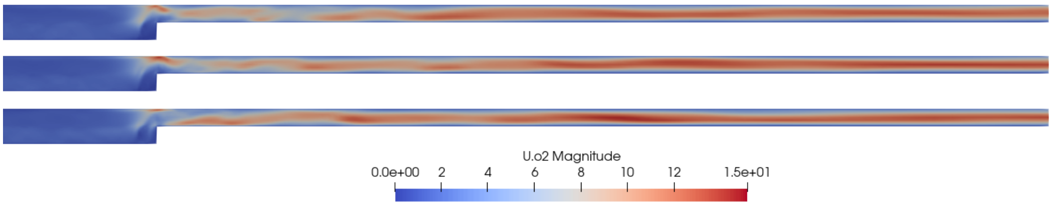

Figure E.16: The transient flow at the outlet, for the slug flow. From top to bottom is the flow at the minimum, mid and maximum point. The parameter illustrated is u_{O_2}.

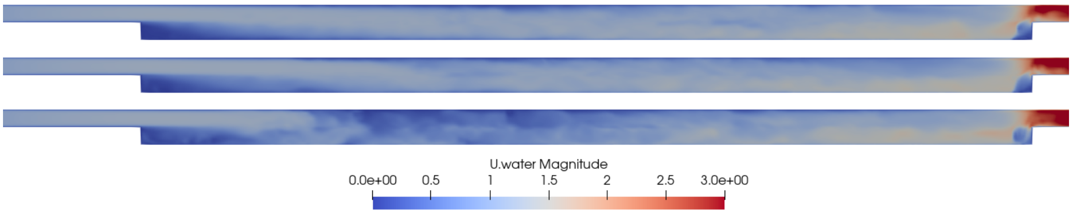

Figure E.17: The transient flow in the PEMEC, for the slug flow. From top to bottom is the flow at the minimum, mid and maximum point. The parameter illustrated is u_{H_2O}.

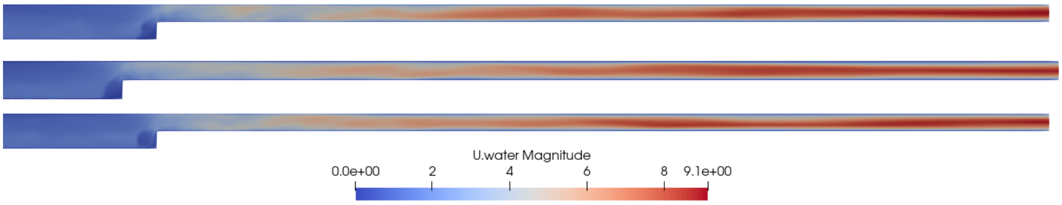

Figure E.18: The transient flow at the outlet, for the slug flow. From top to bottom is the flow at the minimum, mid and maximum point. The parameter illustrated is u_{H_2O}.

Appendix F

Transient Temperature Distribution

In this appendix, the transient temperature distribution from section 4.6 on page 40 is illustrated. Figure F.1 illustrates T_{H_2O} at three different time stamps with the bottom figure illustrating $\langle T_{H_2O} \rangle$. Figure F.2 illustrates the same, but for T_{O_2} instead.

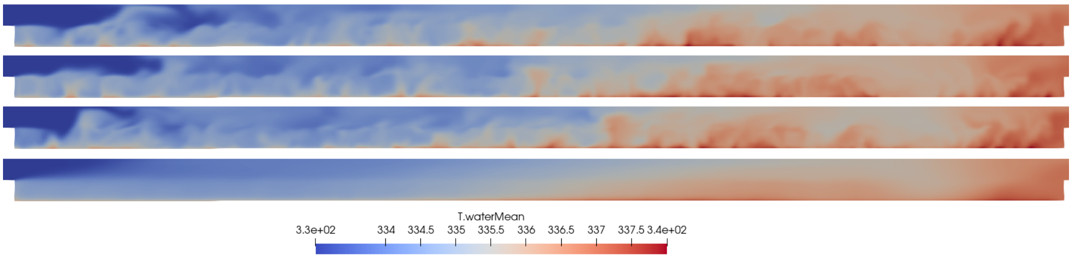

Figure F.1: Transient water temperature distribution. The three first figures illustrate the transient water temperature, and the bottom figure illustrates the time-averaged.

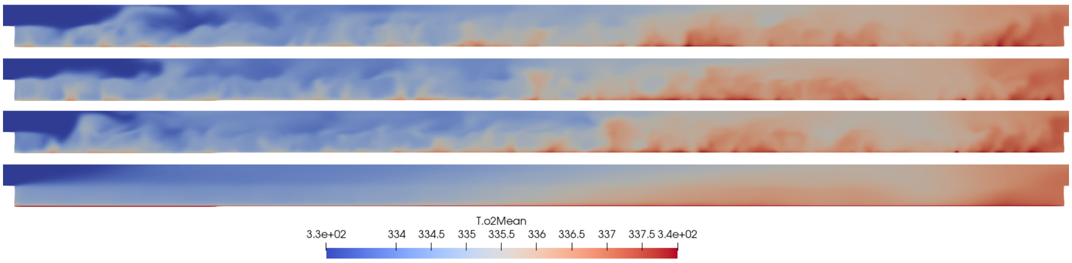

Figure F.2: Transient oxygen temperature distribution. The three first figures illustrate the transient oxygen temperature, and the bottom figure illustrates the time-averaged.